

Assessing synergistic radar and radiometer capability in retrieving ice cloud microphysics based on hybrid Bayesian algorithms

Yuli Liu¹ and Gerald Mace¹

¹University of Utah

November 26, 2022

Abstract

The 2017 National Academy of Sciences Decadal Survey highlighted several high priority objectives to be pursued during the next decadal timeframe, and the next-generation Cloud Convection Precipitation (CCP) observing system is thereby contemplated. In this study, we investigate the capability for ice cloud remote sensing of two CCP candidate observing systems that include a W-band cloud radar and a submillimeter-wave radiometer by developing hybrid Bayesian algorithms for the active-only, passive-only, and synergistic retrievals. The hybrid Bayesian algorithms combine the Bayesian MCI and optimization process to retrieve quantities and uncertainty estimates. The radar-only retrievals employ an optimal estimation methodology, while the radiometer-involved retrievals employ ensemble approaches to maximize the posterior probability density function. The a priori information is obtained from the Tropical Composition, Cloud and Climate Coupling (TC4) in situ data and CloudSat radar observations. Simulation experiments are conducted to evaluate the retrieval accuracies by comparing the retrieved parameters with the known values. The experiment results suggest that the radiometer measurements provide little information on the vertical distributions of ice cloud microphysics. Radar observations have better capacity for retrieving water content compared to particle number concentration. The synergistic information is demonstrated to be helpful in improving retrieval accuracies, especially for the ice water path retrievals. The end-to-end simulation experiments also provide a framework that could be extended to the inclusion of other remote sensors to further assess the CCP observing system in future studies.

1 **Assessing synergistic radar and radiometer capability**
2 **in retrieving ice cloud microphysics based on hybrid**
3 **Bayesian algorithms**

4 **Yuli Liu¹, Gerald G. Mace¹**

5 ¹University of Utah

6 **Key Points:**

- 7 • We develop hybrid Bayesian algorithms for synergistic radar and radiometer re-
8 trievals of ice cloud microphysics
9 • The algorithms combine Bayesian Monte Carlo Integration and different optimiza-
10 tion methods to retrieve quantities and uncertainty estimations
11 • We conduct simulated experiments to quantitatively assess the objective remote sen-
12 sors capability in ice cloud remote sensing

Abstract

The 2017 National Academy of Sciences Decadal Survey highlighted several high priority objectives to be pursued during the next decadal timeframe, and the next-generation Cloud Convection Precipitation (CCP) observing system is thereby contemplated. In this study, we investigate the capability for ice cloud remote sensing of two CCP candidate observing systems that include a W-band cloud radar and a submillimeter-wave radiometer by developing hybrid Bayesian algorithms for the active-only, passive-only, and synergistic retrievals. The hybrid Bayesian algorithms combine the Bayesian MCI and optimization process to retrieve quantities and uncertainty estimates. The radar-only retrievals employ an optimal estimation methodology, while the radiometer-involved retrievals employ ensemble approaches to maximize the posterior probability density function. The a priori information is obtained from the Tropical Composition, Cloud and Climate Coupling (TC4) in situ data and CloudSat radar observations. Simulation experiments are conducted to evaluate the retrieval accuracies by comparing the retrieved parameters with the known values. The experiment results suggest that the radiometer measurements provide little information on the vertical distributions of ice cloud microphysics. Radar observations have better capacity for retrieving water content compared to particle number concentration. The synergistic information is demonstrated to be helpful in improving retrieval accuracies, especially for the ice water path retrievals. The end-to-end simulation experiments also provide a framework that could be extended to the inclusion of other remote sensors to further assess the CCP observing system in future studies.

1 Introduction

The 2017 earth science decadal survey (Board et al., 2019) identified five designated foundational observations to be pursued during the 2017-2027 time frame, and the Aerosols (A), and Clouds, Convection, and Precipitation (CCP) are included as designated observables (DOs). In the preformulation study, the A and CCP DOs were merged to exploit synergies in the measurement systems. The objective of the preformulation study was to identify measurables that can achieve the science objectives of the DOs. As such, the study identified observing system architectures that maximize science benefit while limiting cost and risk. To narrow in on a set of viable architectures, the ACCP study relied on a suite of Observing System Simulation Experiments (OSSEs) aimed at addressing pixel-level retrieval uncertainties and sampling trade-offs for various geophysical variables that were deemed important to achieving science goals.

The properties of ice clouds are among the critical geophysical variables in the CCP science objectives. Ice clouds play a significant role in modulating the energy budget of the earth system by absorbing upwelling long-wave radiation emitted from the lower troposphere and reflecting incoming solar short-wave radiation (Liou, 1986; Su et al., 2017). Studies suggest that ice clouds are a net heat source to the climate system (Stephens & Webster, 1984; Berry & Mace, 2014) while contributing a positive feedback to the climate system (Zelinka & Hartmann, 2011).

The radiative effects of ice clouds depend on the vertically integrated and the vertical distribution of ice particle characteristics (Ackerman et al., 1988; Hartmann & Berry, 2017). Microwave RADio Detection And Ranging (RADAR) and the submillimeter-wave radiometry are two critical techniques for ice cloud remote sensing that are strongly synergistic when combined (Buehler et al., 2012). The microwave radar provides radar reflectivity that constrain ice cloud microphysical quantities in a vertically resolved sense while the submillimeter-wave radiometer constrains integrated mass and particle size. These two techniques are also highly complementary. The nadir looking microwave cloud radar provides high resolution of ice cloud vertical profiles but are limited to the along-track measurements, whereas the scanning submillimeter-wave radiometer has a wide

64 swath but provides limited information about cloud vertical structure. Combing the strength
 65 of both observing sensors enhances our capability to better acquire ice cloud spatial dis-
 66 tributions.

67 Several retrieval algorithms have been developed specifically for ice cloud radiom-
 68 etry studies. All applicable algorithms that could be roughly classified as statistical ap-
 69 proaches and optimization approaches are under the framework of Bayes theorem. The
 70 statistical approaches, including the Bayesian Monte Carlo Integration (MCI) (Evans et
 71 al., 2002, 2005) and the Neural Network (Jimenez et al., 2007; Brath et al., 2018), builds
 72 up an a priori database by randomly generating atmospheric/cloud cases according to
 73 a prior probability density function (PDF) and simulating instrument-specific measure-
 74 ments. The retrieval results are obtained through interpolation over the precalculated
 75 databases. To solve the sparsity of database cases in the measurement space, optimiza-
 76 tion algorithms are developed to maximize the posterior PDF. Evans et al. (2012) ap-
 77 plied the Optimal Estimation Method (OEM) and Markov Chain Monte Carlo (MCMC)
 78 to retrieve ice cloud profiles from the Compact Scanning Submillimeter Imaging Radiome-
 79 ter (CoSSIR; (Evans et al., 2005)) observations during the Tropical Composition, Cloud
 80 and Climate Coupling (TC4; (Toon et al., 2010)) experiment. Liu et al. (2018) proposed
 81 an ensemble estimation algorithm that does not use the gradient information but always
 82 relies on estimating posterior PDF to minimize the cost function. For the combined radar
 83 and radiometer retrievals, Pfreunds Schuh et al. (2020) developed OEM algorithms for the
 84 upcoming Ice Cloud Imager radiometer (Kangas et al., 2014) and a conceptual W-band
 85 cloud radar to investigate to synergies between the active and passive observations.

86 The objective of this paper is to develop candidate algorithms for synergistic radar
 87 and radiometer retrievals to quantitatively assess the capability of sensing designated ice
 88 cloud geophysical variables for the next-generation ACCP observing system. The algo-
 89 rithms for active-only, passive-only, and combined retrievals use a hybrid Bayesian frame-
 90 work, which combines the Bayesian MCI and optimization process to retrieve ice cloud
 91 quantities with uncertainty estimates. This paper is structured as follows: Section 2 de-
 92 scribes the objective submillimeter-wave radiometer and the reference cloud sense used
 93 for testing the retrieval accuracies; Section 3 describes the hybrid Bayesian algorithms
 94 for the radar-only, radiometer-only, and synergistic retrievals in detail; Section 4 describes
 95 the a priori database that is derived from in situ data and CloudSat Cloud Profiling Radar
 96 observations; Section 5 conducts the retrieval simulation experiments and quantitatively
 97 evaluates the retrieval performance; and finally, Section 6 presents the summaries and
 98 conclusions.

99 **2 Simulated observations**

100 **2.1 remote sensors**

101 The remote sensors we evaluate in this study include a W-Band radar and a (sub)millimeter
 102 wave radiometer both of which are candidates in the ACCP observing system. The W-
 103 band cloud radar that we assume here is similar to the Cloud Profiling Radar (CPR) in
 104 the CloudSat satellite (Stephens et al., 2008; Tanelli et al., 2008). The passive radiome-
 105 ter we consider is conical-scanning with 16 horizontally polarized channels at the frequen-
 106 cies of 118 1.1, 118 1.5, 118 2, 118 5, 183 1, 183 2, 183 3, 183 6, 240, 310, 380 0.75,
 107 380 1.5, 380 3, 380 6, 660, and 880 GHz. Most frequency channels are centered on wa-
 108 ter vapor absorption lines. This radiometer has a 45 off-nadir angle and a 750 km swath
 109 width. Figure 1 shows the simulated clear-sky brightness temperature (BT) spectrum
 110 for a tropical atmospheric scenario. All passive sensors channel positions and a detailed
 111 view of the double sidebands located on either side of a central frequency are shown.

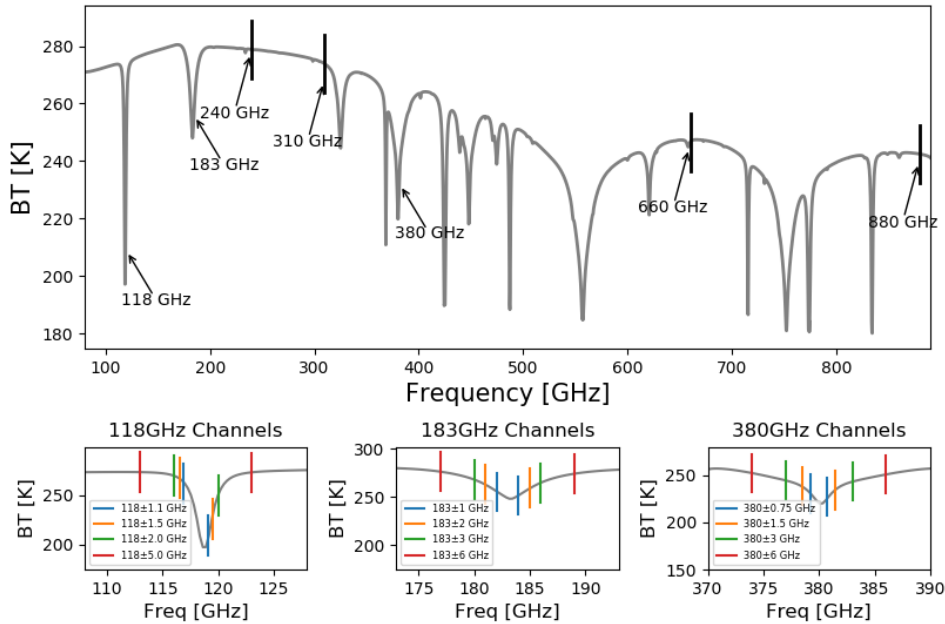


Figure 1. Simulated clear-sky brightness temperature spectrum at a tropical atmospheric scenario. All ACCP radiometer channel positions and a detailed view of the double sidebands located on either side of a central frequency are present.

112

2.2 reference cloud scenes

113

114

115

116

117

118

119

120

121

122

123

124

125

126

127

128

129

The major consideration in selecting reference cloud scenes is to guarantee its independence with the cloud microphysics in the a priori retrieval database (see more details in Section 4.2), but also to keep the two datasets consistent in a geographic context. In this study, we select cloud profiles along a tropical transect that are simulated using the Environment and Climate Change Canada (ECCC) model (Chen et al., 2018) and those profiles were made available to the ACCP Science Impacts Team (Kollias, personal communication). The model outputs provide the water content and number concentration for cloud ice, snow, liquid cloud, and rain, but only frozen cloud particles (ice and snow) are used in this study since only ice cloud vertical profiles are presently synthesized in the a priori database (refer to Section 4.2 for more details). In the numerical models, cloud ice is generally characterized by high particle number densities and small particle sizes, while snow is characterized by lower number densities and larger particle size. The model outputs have a vertical resolution of 100-meter, but all atmospheric profiles and microphysical cloud parameters are interpolated according to a range gate spacing similar to CloudSat. We select a transect among the ECCC mode outputs which covers the region between -2.5 and 9 latitude. The selected cloud scenes for testing contain 1280 atmosphere/cloud profiles in total.

130

131

132

133

134

135

We develop the forward model for both active and passive simulations based on the Atmospheric Radiative Transfer Simulator (Buehler et al., 2005; Eriksson et al., 2011). ARTS is dedicated to radiative transfer calculations in the millimeter and submillimeter spectral range. The recently published Single Scattering Databases (SSD) for total random orientation (Eriksson et al., 2018) and azimuthal random orientation (Brath et al., 2020) make it more powerful in investigating various ice cloud properties. The ARTS

136 forward model developed in this study employs the two-moment scheme that requires
 137 both water content and number concentration as input to describe the particle size dis-
 138 tribution (PSD). The frozen particles are assumed to be randomly orientated, and the
 139 scattering properties for both ice and snow are approximated by the EvansSnow habit
 140 from the ARTS SSD database. The forward model used during the optimization pro-
 141 cess applies the same particle habit since the uncertainties introduced by various par-
 142 ticle habits are not investigated in this study.

143 Figure 2 shows the vertical distribution of water content and number concentra-
 144 tion for cloud ice and snow particles along the selected latitudinal transect and the cor-
 145 responding W-band radar simulations. The radar minimum sensitivity is set to be -30
 146 dBz, thus some thin clouds are not detected. Compared to the number concentration,
 147 the radar simulations show more tendency to follow the variation of IWC. Figure 3 shows
 148 the IWP and the corresponding BT simulations for all ACCP radiometer channels. A
 149 clear relationship between the IWP and BT depression is evident. The channels with higher
 150 central frequency are more sensitive to the change of water path. For the double side-
 151 bands centered on the same center frequency, the large frequency-offset channels show
 152 higher brightness temperature values in clear sky conditions, and they have larger BT
 153 depressions when encountering thick ice cloud layers.

154 Figure 4 shows the scatterplot of the BT difference between simulations in the clear
 155 sky and cloudy conditions versus IWP for different channels. The 118 GHz channels demon-
 156 strate sensitivity when the IWP is over 10^3g/m^2 . This is not surprising since the 118 GHz
 157 channels are primely designed for sensing temperature profiles. For the 183 GHz and 380
 158 GHz channels, the biggest BT differences are up to 50 K and 80 K, respectively. Also,
 159 the 380 GHz channels simulations show more separation for the same IWP values, im-
 160 plying that the high-frequency channels are more sensitive to the IWC vertical distri-
 161 butions. The BT difference for the 660 GHz and 880GHz window channels are notice-
 162 able even when the IWP is below 100g/m^2 , and the difference values could up to 110
 163 K under our reference cloud sense. These two channels make the ACCP radiometer ca-
 164 pable of sensing thin clouds that are usually composed of small particles. However, both
 165 660 and 880 GHz show signs of saturation for IWP in excess of 10^3g/m^2 .

166 3 Hybrid Bayesian algorithms

167 We developed different hybrid Bayesian algorithms for the radar-only, radiometer-
 168 only, and synergistic retrievals of ice cloud parameters from the reference cloud scenes.
 169 All hybrid algorithms combine Bayesian MCI with optimization processes to retrieve quan-
 170 tities and uncertainty estimates. Bayesian MCI introduces the prior information by gen-
 171 erating an ensemble of atmospheric cases that are distributed according to the prior PDF
 172 to build up the retrieval database, which is highly efficient since the retrievals are done
 173 by interpolating the database cases and no more forward model calculations are required.
 174 By assuming the uncertainties for different measurement variables to be independent,
 175 the conditional PDF, which is also the posterior PDF, can be written as:

$$176 \quad p_{cond}(x|y_{obs}) \propto \exp\left(-\frac{1}{2}\chi^2\right) \quad \chi^2 = \sum_{j=1}^M \frac{(y_{sim,j} - y_{obs,j})^2}{\sigma_j^2} \quad (1)$$

177 where p_{cond} is the conditional probability of the measurement vector y_{obs} given a par-
 178 ticular atmospheric state x , y_{sim} is the simulated observation vector, and σ_j^2 is the un-
 179 certainty of observation and forward model. The retrieved quantities and uncertainties
 180 are calculated by Monte Carlo Integration over the state vectors to find the mean vec-

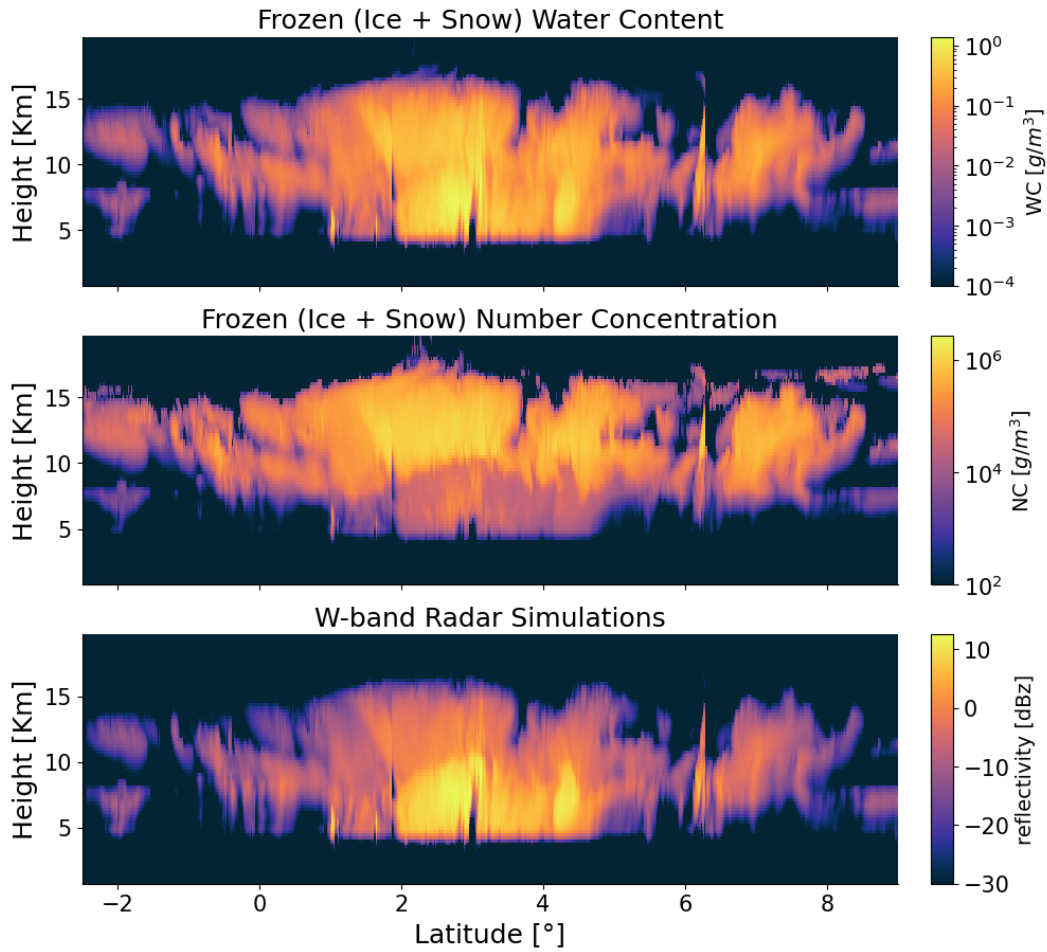


Figure 2. Vertical distribution of water content (WC) and number concentration (NC) for ice and snow particles along the selected latitudinal transect and the corresponding W-band radar reflectivity simulations. The radar simulations are computed using Atmospheric Radiative Transfer Simulator (ARTS) forward model.

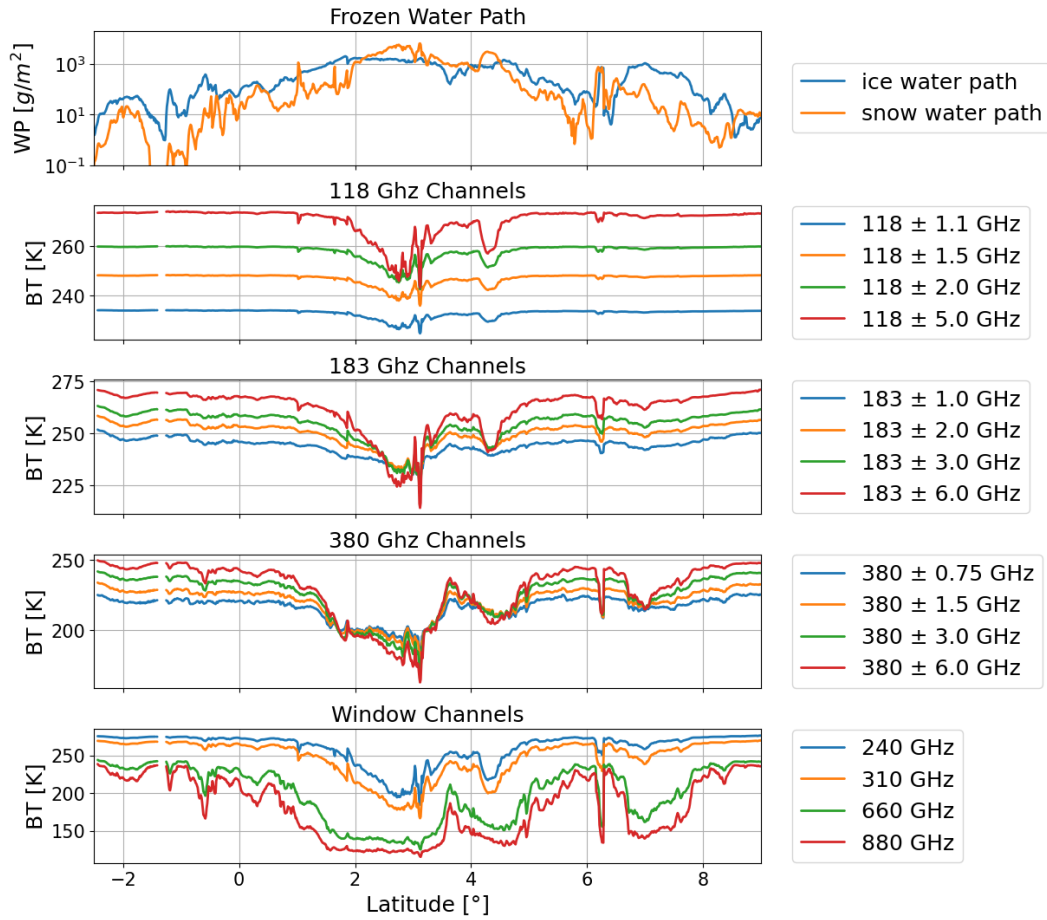


Figure 3. Integrated water content for ice and snow particles for the selected latitudinal transect and the corresponding brightness temperature simulations for all ACCP radiometer channels.

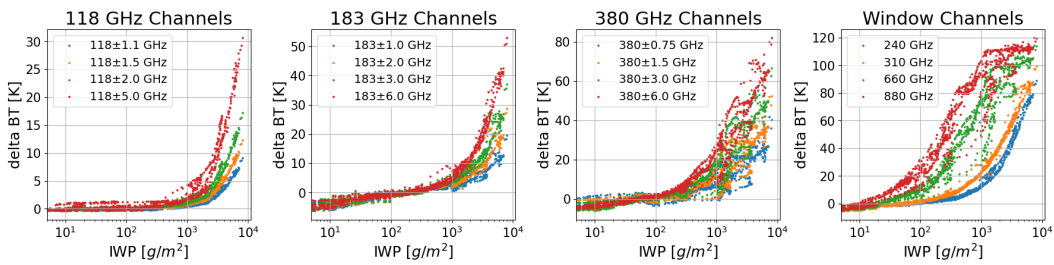


Figure 4. Scatterplot of the brightness temperature difference between simulations in the clear sky and cloudy conditions as a function of ice water path for all ACCP radiometer channels.

181 tor and the associated standard deviation:

$$\begin{aligned}
 \bar{x} &= \frac{\sum_i x_i \exp(-\frac{1}{2}\chi_i^2)}{\sum_i \exp(-\frac{1}{2}\chi_i^2)} \\
 \sigma_{\bar{x}} &= \sqrt{\frac{\sum_i (x_i - \bar{x})^2 \exp(-\frac{1}{2}\chi_i^2)}{\sum_i \exp(-\frac{1}{2}\chi_i^2)}}
 \end{aligned}
 \tag{2}$$

183 The biggest problem for the Bayesian MCI is the sparsity in the measurement space
 184 for a retrieval database with a finite number of cases. If we increase the length of the
 185 observation vector or decrease the measurement uncertainties, the number of database
 186 cases that match the observation vector become smaller and the Bayesian MCI fails. When
 187 this happens, the optimization process is begun to maximize the posterior PDF.

188 3.1 Radar-only retrievals

189 The optimization algorithm for radar retrievals is based on the robust and efficient
 190 OEM algorithm. OEM assumes that the forward model is moderately nonlinear and that
 191 both prior PDF and conditional PDF are Gaussians. OEM maximizes the posterior PDF
 192 by minimizing the following cost function:

$$J = (F(x) - y)^T S_y^{-1} (F(x) - y) + (x - x_a)^T S_a^{-1} (x - x_a)
 \tag{3}$$

194 where $F(x)$ is the forward model simulation, S_y and S_a are the covariance matrix for
 195 the measurement and prior uncertainties. In this study, the Levenberg-Marquardt min-
 196 imization method (Rodgers, 2000) is implemented, and the required Jacobian matrix is
 197 calculated by perturbing the cloud microphysical parameters in each pixel. The initial
 198 state vector is constructed by implementing Bayesian MCI to each reflectivity value in
 199 different layers using the precalculated radar retrieval database described in Section 4.1.
 200 The posterior error covariance matrix specified below is used to characterize the retrieval
 201 uncertainties:

$$S = (S_a^{-1} + K^T S_y^{-1} K)^{-1}
 \tag{4}$$

203 where K is the Jacobian matrix to linearize the forward model. This covariance matrix
 204 is also derived based on the local Gaussian approximation and the forward model lin-
 205 earization assumption. The relative change of the cost function J is considered as the
 206 criteria for testing converge. The OEM optimization terminates if the relative change
 207 of J is below a specified threshold or the algorithm is over a certain number of iterations.

208 3.2 Radiometer-involved retrievals

209 The radiometer-involved retrievals that include the passive-only and the synergis-
 210 tic retrievals that also include radar do not use the OEM algorithm since it does not con-
 211 verge if the Jacobian matrix for BT is computed by perturbing vertically resolved ice cloud
 212 microphysical parameters. The applicable Jacobian matrix is usually obtained in two dif-
 213 ferent ways. The first one is based on the adjoint modeling of radiative transfer. The ad-
 214 joint approach is applied in some models like SHDOMPPDA (Evans, 2007), but it is not
 215 available in the ARTS forward model used here. A second approach is developed by the
 216 ARTS community, which does not calculate the BT sensitivity to the ice cloud micro-
 217 physical parameters but to the scaling parameters in a normalized particle size distri-
 218 bution formalism proposed by Delanoe et al. (2005). In this study, however, since the
 219 in situ data are analyzed based on different PSD scheme and the a priori information
 220 is specified in terms of microphysical parameters, this approach is also not employed. In-
 221 stead, we employ the ensemble approaches to handle the radiometer-involved optimiza-
 222 tions. The ensemble approaches are discussed in the following two subsections.

223 **3.2.1 synergistic retrievals**

224 The synergistic radar and radiometer retrievals are done by extending the radar
 225 OEM algorithm to add the radiometer observations. The radar OEM algorithm provides
 226 the retrieved values and the associated uncertainty estimations. Following this step, the
 227 Cholesky decomposition is implemented on the covariance matrix and an ensemble of
 228 random cases with a correlated Gaussian distribution around the radar retrieved vec-
 229 tor is generated. This is done by decomposing the covariance matrix into a lower trian-
 230 gular form and then multiplying the result by the standard normalized vectors. The cor-
 231 responding BT simulations are subsequently computed by the radiative transfer model.
 232 The final retrieval results are calculated by the Bayesian MCI after evaluating the simu-
 233 lated cases according to their distance to the BT measurement vector, as indicated in
 234 Eq. (2).

235 **3.2.2 radiometer-only retrievals**

236 We employ the Ensemble Estimation Algorithm (EnEA) as the optimization proce-
 237 dure for radiometer-only retrievals. The EnEA was first proposed by Liu et al. (2018),
 238 and we continue to develop it as an optimization methodology. This algorithm is nom-
 239 inally proposed for the submillimeter-wave radiometer, but it is generally applicable to
 240 other remote sensors as well. The EnEA algorithm has advantages in the following as-
 241 pects. First, the algorithm does not rely on gradient information to move forward. Since
 242 the Jacobian calculations are either complex to implement or computationally expen-
 243 sive, the EnEAs characteristic of no Jacobian dependence makes it suitable for ice cloud
 244 profile retrievals that have high dimensional state vectors using advanced radiative trans-
 245 fer models. Second, the EnEA is always under the Bayesian MCI framework. This frame-
 246 work not only provides a solid theoretical basis but also offers a straightforward way to
 247 estimate the retrieval uncertainty associated with each retrieved quantity.

248 The EnEA stochastically explores the state vector space by sampling an explicit
 249 probability distribution function estimated from promising weighted cases found so far
 250 from the perspective of Bayesian MCI. The algorithm consists of two modules: the es-
 251 timation module numerically estimates the unknown continuous posterior PDF using the
 252 discrete cases with posterior values in the last ensemble, and the sampling module syn-
 253 thesized new cases according to the accumulated PDF. Started from the situation where
 254 too few a priori database cases matching the observations, the EnEA artificially inflates
 255 the measurement uncertainties so that there are enough matches between the observa-
 256 tion vector and the BT simulations from the a priori profiles. The algorithm then com-
 257 putes the posterior values and applies a reselect procedure to make the weights of selected
 258 cases equivalent again. The covariance matrix of selected atmosphere profiles is calcu-
 259 lated, and then it is used in a principal components method to generate new MCI cases
 260 having a Gaussian distribution around each of the selected cases, with the Gaussian de-
 261 viates scaling with the previous posterior PDF. Once a new ensemble of random cases
 262 is synthesized and the corresponding BT is simulated, the algorithm evaluates these cases
 263 based on the prior PDF and likelihood PDF, and the optimization cycle starts again.
 264 As the iteration proceeds, the ensemble evolves and gradually becomes concentrated in
 265 the most likely area, compensating for the sparse distribution of the original retrieval
 266 database. The iteration stops when meeting a specified criterion, and the remaining cases
 267 in the last ensemble are used to calculate the mean parameter values (retrieved values)
 268 and standard deviations (retrieved uncertainties) by Bayesian MCI. More details about
 269 the algorithm implementation can be found in (Liu et al., 2018).

270 Several components in the EnEA method are updated in this study to make this
 271 algorithm more applicable in actual retrievals. Firstly, instead of only relying on the Global
 272 Environmental Multiscale Model (Cote & Staniforth, 1998) output, we build up a pre-
 273 calculated retrieval database according to the a priori PDF derived from in situ mea-

274 surements and space-borne radar measurements to make the synthesized ice cloud pro-
 275 files more realistic and representative (Liu & Mace, 2020). Secondly, the retrieval per-
 276 formance of the EnEA is now evaluated by keeping the ice cloud vertical profiles in the
 277 a priori database and the ones used for testing to be completely independent. Thirdly,
 278 a new strategy is applied to deal with the regularization term that constrains the syn-
 279 thesized profiles to follow our prior knowledge. Liu et al. (2018) employed a normally
 280 distributed prior PDF which uses the Bayesian MCI estimates that are computed from
 281 the initial retrieval database by inflating measurement noise as the mean vector. The
 282 drawbacks of the method are twofold. First, the a priori PDF is required to be Gaus-
 283 sian, which made the EnEA less attractive since the algorithm is intended to handle the
 284 retrievals where prior PDF could have any functional form. Second, this method depends
 285 on a parameter to characterize the strength of the regularization. This parameter needs
 286 to be tuned experimentally, and the tuning itself could be a difficult optimization prob-
 287 lem. In this study, the control vector transformation method applied in Evans et al. (2012)
 288 is employed. This allows the implementation of prior constraints even when the real a
 289 priori distribution is highly non-Gaussian. This method will be discussed in detail in Sec-
 290 tion 4.2.

291 4 Prior information

292 The key element in implementing the Bayesian MCI is to build up the retrieval database,
 293 which generally consists of two steps: creating random atmosphere and ice cloud prop-
 294 erties that are distributed according to the prior PDF and computing the simulated radar
 295 reflectivity or BT using the forward model. In this study, we separately develop two prior
 296 databases for radar and radiometer retrievals using prior information from in situ mea-
 297 surements and CloudSat observations.

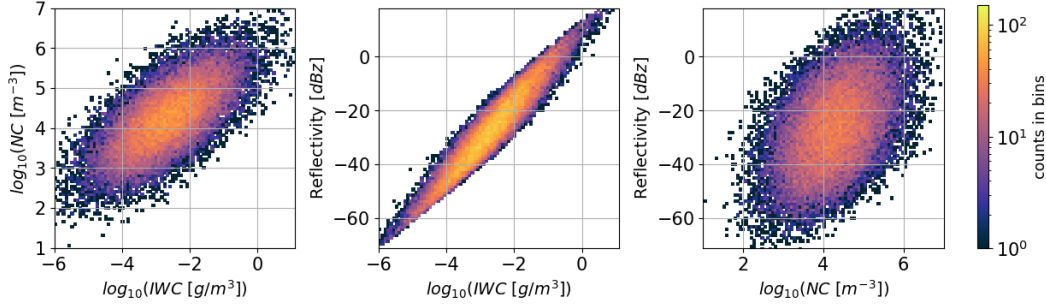
298 4.1 Radar retrieval database

299 The realistic ice cloud microphysical probability distributions used for building up
 300 the radar retrieval database is obtained from the in situ data from instruments flown in
 301 the TC4 campaign. The in situ ice particle size distribution (PSD) is obtained from the
 302 two-dimensional stereo (2D-S) probe and the precipitation imaging probe (PIP). The bi-
 303 modal PSD scheme which approximates both small and large particle distribution modes
 304 by gamma functions is used to fit the in situ data, and the ice cloud parameters, includ-
 305 ing ice water content (IWC), number concentration (NC), and particle size are derived.
 306 More details about TC4 in situ analysis could be found in (Liu & Mace, 2020). A multi-
 307 variant Gaussian distribution in temperature, $\ln(IWC)$, and $\ln(NC)$ is used to capture
 308 the in situ statistics, using the prior idea that the microphysical parameters are approx-
 309 imately lognormally distributed. Using a multi-variant Gaussian function shows several
 310 advantages in generalizing the in situ statistics: first, it specifies the microphysical PDF
 311 using a few parameters; second, it facilitates the following radar OEM algorithm, which
 312 explicitly requires a normally distributed prior PDF; third, it reasonably covers the space
 313 where the in situ probes fail to detect, which is important since the random cases need
 314 to completely cover the possible parameter range. The parameters for the TC4 multi-
 315 variant Gaussian function are summarized in Table 1. A number of random cases (30,000
 316 cases in this study) are sampled from the Gaussian function, and the ARTS radar for-
 317 ward model is used to simulate the reflectivity for each random case.

318 Figure 5 shows the two-dimensional histogram for the microphysical quantities and
 319 reflectivity simulations in the radar retrieval database. The middle panel and the right
 320 panel indicate that the radar reflectivity simulations have a strong correlation with IWC
 321 in the whole range, but its correlation with NC is much weaker.

Table 1. Ice particle microphysical statistics defining the a priori Gaussian probability distribution derived from the TC4 in situ data

| | $\ln(\text{IWC})$ (g/m^3) | $\ln(\text{NC})$ ($/\text{m}^3$) | Temperature (K) |
|--------------------|---|------------------------------------|-----------------------------|
| <i>mean</i> | -6.04 | 9.88 | 231.07 |
| <i>std</i> | 2.45 | 1.81 | 12.41 |
| <i>correlation</i> | $\rho_{\ln(iwc)-\ln(nc)} = 0.69$ | $\rho_{\ln(iwc)-tp} = 0.17$ | $\rho_{\ln(nc)-tp} = -0.10$ |

**Figure 5.** Two-dimensional histogram for the microphysical quantities and the W-band radar reflectivity simulations derived from the random cases in the precalculated radar retrieval database.

4.2 Radiometer retrieval database

Apart from using the TC4 in situ microphysical statistics, we also use the CloudSat observations to acquire the critical coherent vertical correlations to synthesize the random ice cloud profiles for radiometer retrieval database creation. The data we use include CloudSat radar reflectivity, CALIPSO lidar cloud fraction, and the corresponding ECMWF profiles of temperature and relative humidity. The active remote sensing data profiles are combined with the TC4 cloud microphysical probability distributions where we employ the Bayesian MCI algorithm to create vertical profiles of microphysical properties that are consistent with the measurements and the in situ statistics. After that, the cumulative distribution functions (CDFs) and empirical orthogonal functions (EOFs) procedures are applied to capture the complete single-point and two-point statistics and then to create any number of synthetic microphysical and thermodynamic profiles (100,000 profiles in this study) that are statistically consistent with the Bayesian retrieval results. A comprehensive discussion on creating synthetic ice cloud profiles can also be found in Liu and Mace (2020).

As mentioned in section 3.2.2, we employ the control vector transformation method to implement the prior constraint. The CDFs are used to capture the one-point statistics by sorting the variable at different layers from smallest to largest in value and calculating the sum of the assigned equal probabilities up to each datum. The percentile ranks at different layers are transformed into Gaussian derivate matrix using the standard normal cumulative distribution function:

$$\xi_i = \phi^{-1}(R(x_i)) \quad (5)$$

where $\phi(\xi)$ is the standard normal cumulative distribution function, and $R(x_i)$ is the percentile ranks for different parameters at different layers. For a new ensemble, the strength of the prior constraints for different ice cloud profiles is determined by their ξ values. This step allows the implementation of a more realistic prior PDF that is captured by the CDFs.

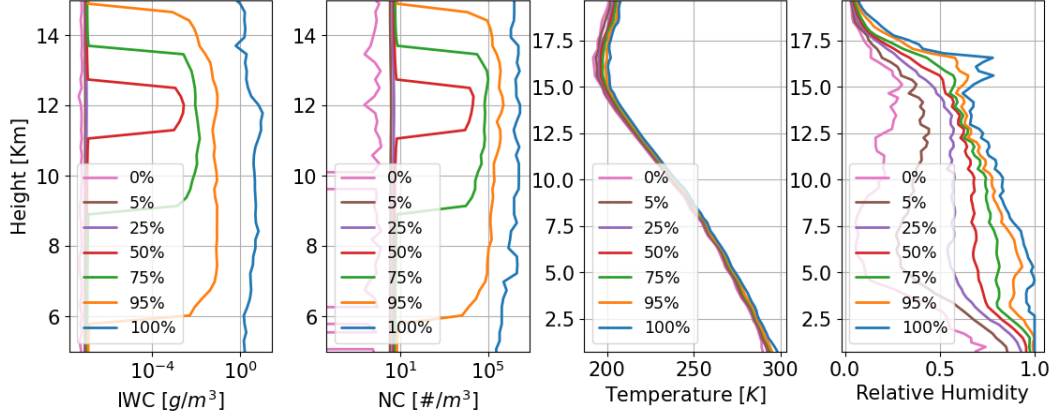


Figure 6. Profiles of ice water content (IWC), number concentration (NC), temperature, and relative humidity for seven percentiles in the cumulative distributions for the random atmospheric/cloud profiles in the precalculated radiometer retrieval database.

348 Figure 6 shows the profiles of IWC, NC, temperature, and relative humidity for seven
 349 percentiles in the cumulative distributions. Layers that are identified as clear are added
 350 with random Gaussian noise to prevent discontinuity in the CDFs. The mean values for
 351 the added IWC and NC noise are 10^{-6}g/m^3 and 10 m^{-3} , respectively. The left two pan-
 352 els show that the a priori IWC profiles cover the range from clear condition to about 10
 353 g/m^3 , and the NC profiles cover the range up to about 10^6m^{-3} . The 50% curve only has
 354 meaningful values in the 11 to 13 km high range, indicating that the ice cloud particles
 355 are mostly concentrated in this region. The 75% curve implying that a large majority
 356 of atmospheric conditions outside the 9 to 14km range are effectively clear. The right
 357 two panels show that the a priori temperature profiles have a small range of tempera-
 358 ture coverage under the tropical atmospheric conditions applied in this study, and the
 359 relative humidity profiles have a large possible range, almost coving the entire possible
 360 values from 0 to 1.

361 The precalculated retrieval database provides a good opportunity for estimating
 362 the degrees of freedoms (DoF) for the ACCP radiometer. The DoF describes the num-
 363 ber of independent pieces of information in the radiometer measurement since some chan-
 364 nels provide redundant information. The DoF is usually calculated as the trace of the
 365 averaging kernel matrix based on the Jacobian matrix (Rodgers, 2000), but a more gen-
 366 eral method described in Eriksson et al. (2020) is employed here since the Jacobian ma-
 367 trix for BT is not available in this study. This method calculates the DoF in the mea-
 368 surement space based on the Empirical Orthogonal Function (EOF) approach. The co-
 369 variance matrix of a set of simulated BT is decomposed using EOF:

$$370 \quad S_y = E\Lambda E^T \quad (6)$$

371 where E is the eigenvector and Λ is the diagonal matrix containing the corresponding
 372 eigenvalues. The Gaussian measurement noise in eigenspace is transformed back using
 373 the same eigen coordinate axes:

$$374 \quad S_\Lambda = ES_\xi E^T \quad (7)$$

375 where S_ξ is the diagonal matrix that contains the square of measurement noise for dif-
 376 ferent channels. The DoF is defined as the number of diagonal elements in S_y that are
 377 larger than the corresponding value in S_Λ in the same place.

378 Figure 7 shows the DoF of the ACCP radiometer as the function of the ice water
 379 path (IWP) and integrated water vapor (IWV). The necessary radiometer measurement

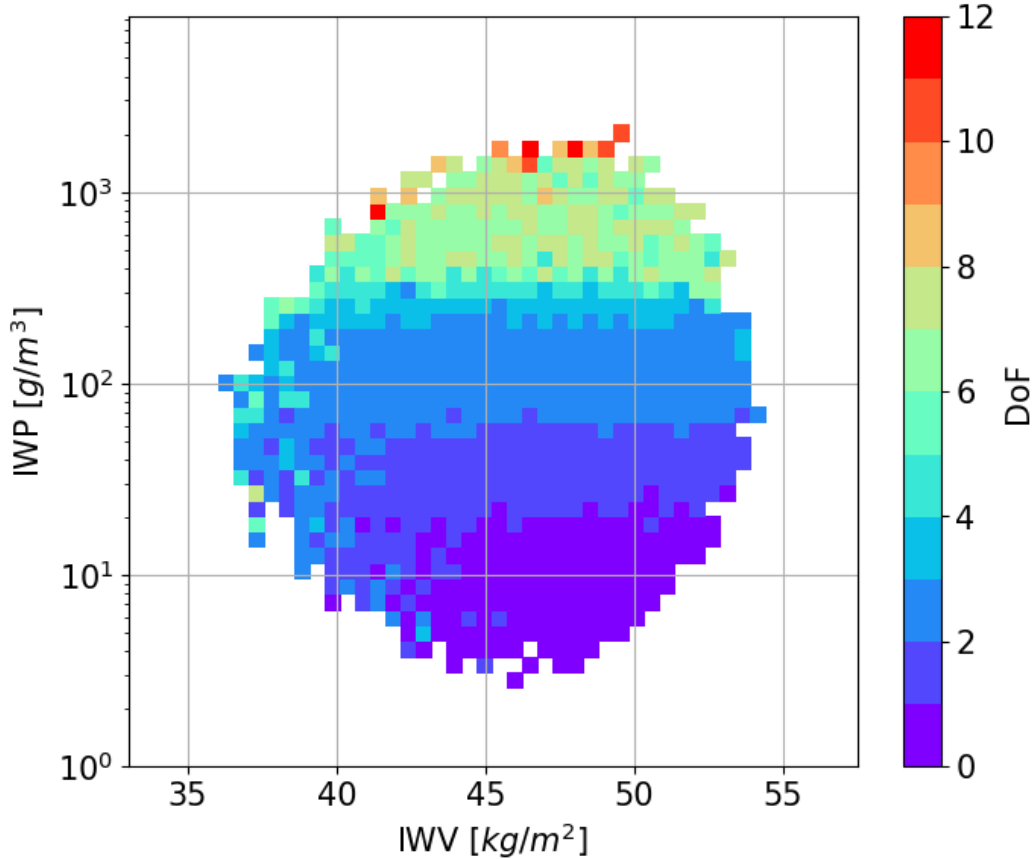


Figure 7. The Degree of Freedoms (DoF) for the ACCP radiometer as the function of the ice water path and integrated water vapor. The DoF is estimated using the radiometer retrieval database that has 100,000 random atmospheric/cloud profiles.

380 noise is configured by referring to the CoSSIR uncertainties that are obtained from cal-
 381 ibration target fluctuation statistics applied in Evans et al. (2012). The double-sideband
 382 channels for 118 GHz, 183 GHz, 380 GHz are set to have uncertainties of 1.5K, 1.6K,
 383 2.3K, and the window channels uncertainties for 240 GHz, 310 GHz, 660 GHz, 880 GHz
 384 are set to be 2.0 K, 2.3 K, 2.5 K, 4.0K, respectively. The DoF is computed only when
 385 the number of random cases in a certain IWV-IWP range is larger than 10 to avoid noise
 386 interference. It can be seen that the DoFs increase with IWP. The DoFs are mostly zero
 387 when the IWP values are smaller than 20 g/m^2 , indicating the ACCP radiometers lim-
 388 itation for IWP detection. The DoFs generally equal to 1 in 20 to 70 IWP range, and
 389 equal to 2 in 70 to 110 IWP range. This analysis is consistent with the plots in Figure
 390 4, which show that only the 660GHz and 880 GHz channels are sensitive to the thin cir-
 391 rus clouds. When IWP is over 300 g/m^2 , the DoF is mostly between 6 to 8, and the DoF
 392 is over 10 very occasionally.

393 5 Retrieval Simulation Experiment and Results

394 We conduct simulated retrieval experiments to evaluate the retrieval accuracy of
 395 ice cloud microphysics for the objective ACCP remote sensors. The simulation obser-
 396 vations for the W-band radar and the submillimeter-wave radiometer under the selected
 397 reference cloud scenes are presented in section 3.1. After adding measurement noise, the

398 simulated observations are input to the hybrid Bayesian algorithms to retrieve desired
 399 quantities and uncertainty estimates. The retrieved parameters are then compared to
 400 the true values to quantitatively assess the retrieval accuracies.

401 Several configurations in the hybrid Bayesian algorithms are summarized here. The
 402 independent Gaussian noise with standard deviation according to the absolute instru-
 403 ment accuracy (1 dBz in this study) is added to the simulated radar observations, but
 404 we applied 4 dBz Gaussian noise in the Bayesian retrievals to also include the forward
 405 model uncertainty that would be realized from imperfect knowledge of ice crystal bulk
 406 density to make the simulation experiments more realistic. The 4 dBz measurement un-
 407 certainty is estimated based on the study of Mace and Benson, 2017. Similarly, the Gaus-
 408 sian noise of 1K is added to the simulated BT in each channel to characterize the ab-
 409 solute accuracy, but more realistic uncertainty estimations specified in section 4.2 are
 410 used in the Bayesian retrievals. For the radar-only retrievals, the initial state vector for
 411 the OEM optimization is stochastically generated layer by layer based on the Bayesian
 412 MCI algorithm using the precalculated radar retrieval database. The retrieval process
 413 precedes from top down, and the generated radar attenuation is used to correct the radar
 414 reflectivity below. The Bayesian MCI retrievals are only applied to the layers with cor-
 415 rected radar reflectivity larger than the minimum sensitivity (-30 dBz). The a priori PDF
 416 used in the OEM optimization only utilizes the statistical Gaussian parameters listed
 417 in Table 1, and the vertical correlations between ice cloud microphysics at different lay-
 418 ers are not considered. For the synergistic retrievals, 500 random cases are generated from
 419 the radar OEM retrieval results to add BT measurement information using Bayesian MCI.
 420 For the radiometer-only retrievals, the ensemble estimation retrievals stop when either
 421 of the two following termination criteria is satisfied: a number of random cases (25 cases
 422 in this study) matching the observations within a specified χ^2 threshold are obtained in
 423 one ensemble, or the number of iterations exceeds a specified value. The χ^2 threshold
 424 is set as $M+4\sqrt{M}$, where M is the number of radiometer channels. This configuration
 425 is based on the fact that the mean value and variance of the χ^2 distribution are M and
 426 2M, respectively. Considering that the radiative transfer simulations for an ensemble of
 427 atmospheric and cloud profiles are computationally intensive, the limitation for the num-
 428 ber of iterations is set to be 3. 500 random cases in the first ensemble and 100 cases in
 429 the following two ensembles are generated to statistically explore the state vector space.

430 Figure 8 and figure 9 show the direct comparison between the true values and the
 431 retrieval results for IWC and NC profiles along the ECCO model transect. The retrieval
 432 results for radar-only, radiometer-only, and combined are presented sequentially. We find
 433 that there is essentially no information regarding the ice cloud vertical profiles in the ra-
 434 diometer measurements. For the active-only retrievals, the retrieved IWC profiles real-
 435 istically reproduce the vertical structure of the reference cloud scenes. The retrieve val-
 436 ues also correspond to the true values in general, even though sometimes the retrievals
 437 tend to underestimate the IWC values, especially on the top of the cloud ranging from
 438 10 km to 15 km in height. By contrast, the active-only retrievals for NC profiles perform
 439 much worse. The true NC values cover the range from $10 m^{-3}$ to over $10^6 m^{-3}$, but the
 440 radar retrievals do not vary too much, usually concentrating around domains in $10^3 m^{-3}$
 441 to $10^5 m^{-3}$ range. The retrieval results again illustrate that the radar measurements are
 442 much more sensitive to the IWC variation of IWC compared to the NC variation. For
 443 the synergistic retrievals, obvious perturbations can be observed for both IWC and NC
 444 profiles and the results become less smooth compared to the radar-only retrievals. The
 445 added radiometer observations tend to correct the IWC underestimation discussed above.

446 Before we further analyze the retrieval results quantitatively, we would like to inves-
 447 tigate the effectiveness of the updated ensemble estimation algorithm first. The algorithm
 448 is now evaluated by ensuring the independence between the vertical profiles in the pre-
 449 calculated prior database and the ones in the reference cloud scenes. Also, a new strat-
 450 egy regarding the addition of prior constraints during ensemble optimization is imple-

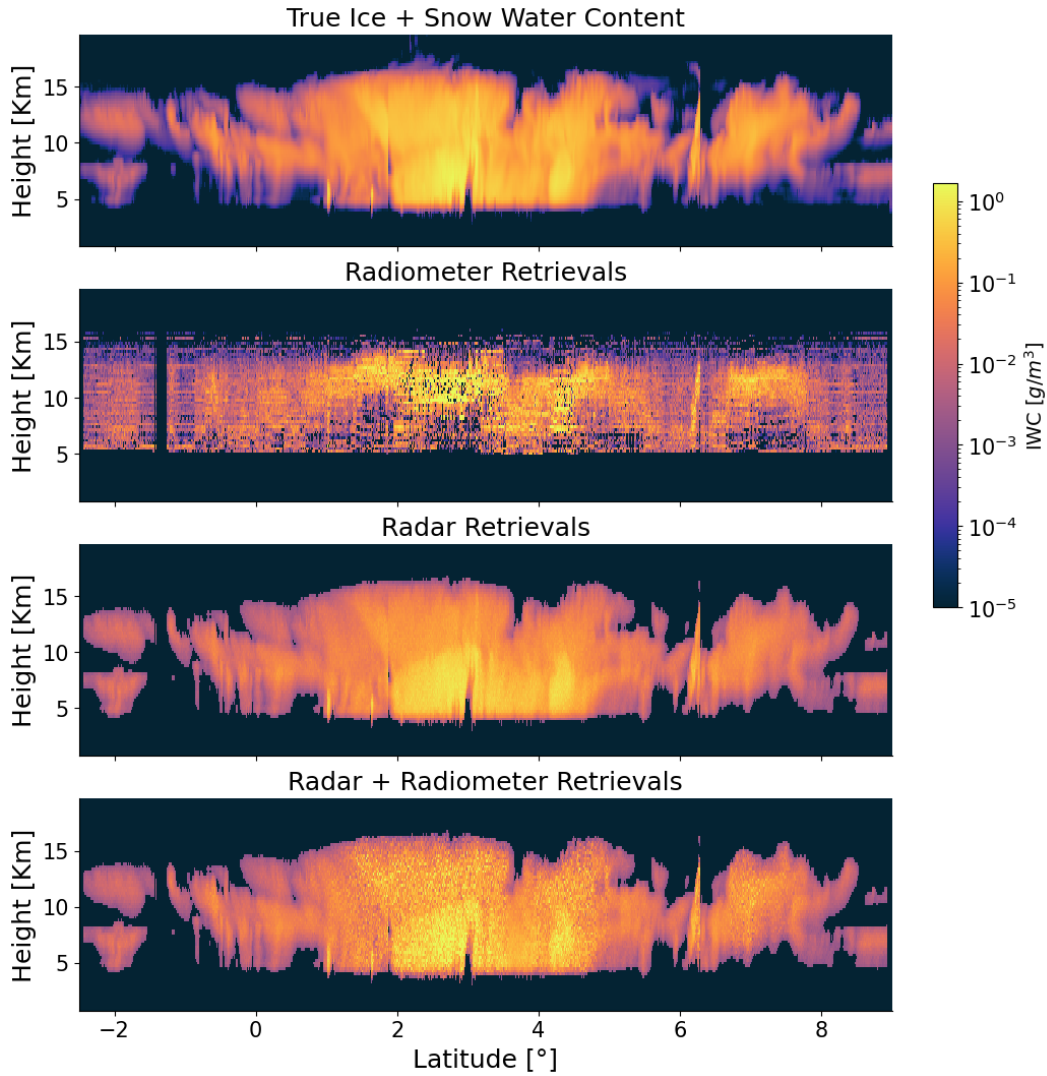


Figure 8. Comparison between the true values and the retrieval results for ice water content profiles along the selected latitude transect. The retrieval results for radar-only, radiometer-only, and combined are presented sequentially.

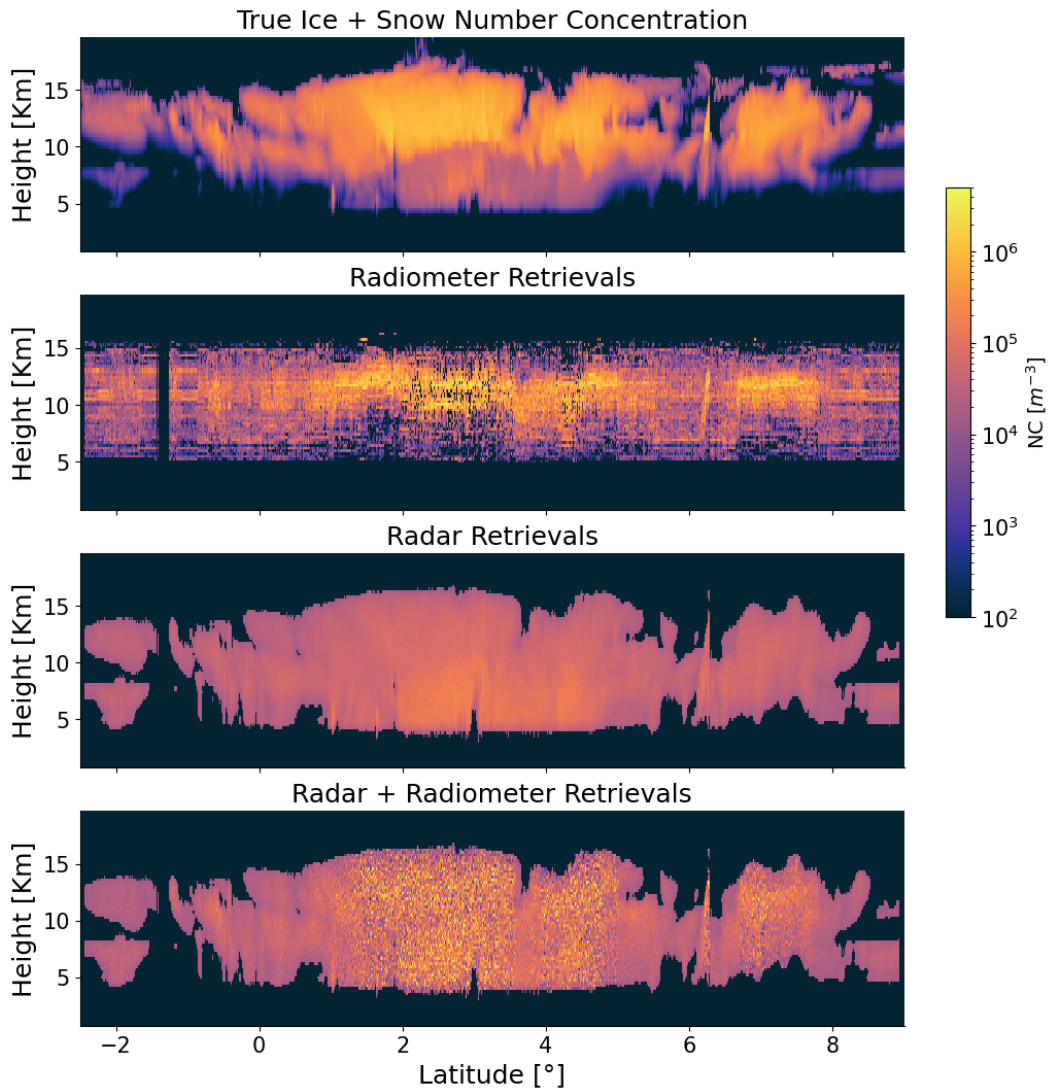


Figure 9. Same as figure 8 but for the retrieval results of number concentration.

451 mented. The top panel of figure 10 shows the comparison of the minimum χ^2 values that
 452 exist in the a priori database and in the last ensemble after optimization. The χ^2 thresh-
 453 old determined by the number of channels is also shown in a dotted grey line. The de-
 454 crease of the cost function is observed over the whole range, indicating that the BT sim-
 455 ulations after optimization better reproduce the measurements within the observation
 456 uncertainties. For most of the input BT measurements, the best database cases have χ^2
 457 values smaller than 100, implying that the prior radiometer database with 100,000 ran-
 458 dom cases covers the BT space well. In these situations, the ensemble estimation algo-
 459 rithm generally reduces the cost function below the specified χ^2 threshold. In the region
 460 between 2 to 4 latitude, the minimum χ^2 values in the a priori database are always over
 461 100, indicating the inevitable sparsity in the measurement space for a database with a
 462 finite number of discrete samples. The corresponding optimized χ^2 values are still large,
 463 but the χ^2 reduction compared to the original values is clear. The bottom panel shows
 464 the comparison of the retrieved IWP before and after the ensemble estimation optimiza-
 465 tion. The retrievals before ensemble optimizations are computed by Bayesian MCI us-
 466 ing the a priori database, even though only a few cases have contributions to the inte-
 467 gration. The true IWP values are shown in a black dot line for reference. We find that
 468 the database retrievals closely follow the true IWP values under the thin ice cloud sit-
 469 uation, but we find a clear underestimation when the IWP is over $10^3 g/m^2$. The database
 470 retrieval accuracies are highly correlated to the χ^2 value shown on the top panel. Some
 471 database retrievals remain the same for different BT input between 2 to 4 latitude, im-
 472 plying the fact that the same database cases respond to different observations during MCI,
 473 which further indicates the sparse distributions in the relevant BT space region. The op-
 474 timization retrievals do not make clear differences when the IWP values are small, but
 475 noticeable improvements are seen when IWP is over a certain value. These figures demon-
 476 strate that the ensemble estimation algorithm effectively improves the retrieval perfor-
 477 mance compared to the retrievals that only depend on the a priori database. Only the
 478 ensemble estimation retrieval results are discussed below.

479 Figure 11 shows the retrieved IWP values for the passive-only, radar-only, and com-
 480 bined retrievals based on the hybrid Bayesian algorithms. The top panel directly com-
 481 pares the retrieved IWP to the true values along the latitudinal transect, and the bot-
 482 tom panel shows the logarithmic errors to make the comparisons clearer. The logarith-
 483 mic error is defined as:

$$484 E_{\log_{10}} = \log_{10}\left(\frac{x_{retrieved}}{x_{true}}\right) \quad (8)$$

485 and the 0 dB logarithmic error represents that the retrieved value and true value are iden-
 486 tical. For the passive-only retrievals, the retrieval errors when IWP is smaller than 100
 487 g/m^2 are high, but the errors become comparable to the active-involved retrievals in other
 488 circumstances. The active-only retrievals show the tendency to overestimate the IWP
 489 for thin clouds but underestimate the thick cloud IWP. The combined retrievals are de-
 490 veloped from the radar OEM results, and substantial improvements in IWP retrieval ac-
 491 curacy can be seen after adding the ACCP BT measurements. Most retrieval errors are
 492 between -0.5 dB and 0.5 dB.

493 Figure 12 shows the mean IWP absolute logarithmic error in each IWP increment
 494 as a function of IWP. As expected, the radiometer-only retrieval errors are large for the
 495 low IWP because the corresponding DoF is very low. The retrieval errors increase when
 496 IWP is over $10^3 g/m^2$, which is primarily because the a priori database does not densely
 497 cover the relevant region. The IWP absolute errors for the radar-only retrievals remain
 498 low for the thin cloud. The errors increase when IWP is over $300 g/m^2$, generally higher
 499 than the passive-only retrievals under the same cloud scenes. The combined retrievals
 500 have significant improvements over the whole range, and the mean errors are mainly around
 501 0.1 dB.

502 Figure 13 shows the scatterplots of the retrieved parameters against the true val-
 503 ues that are colored by density to visualize the retrieval performance. The scatterplots

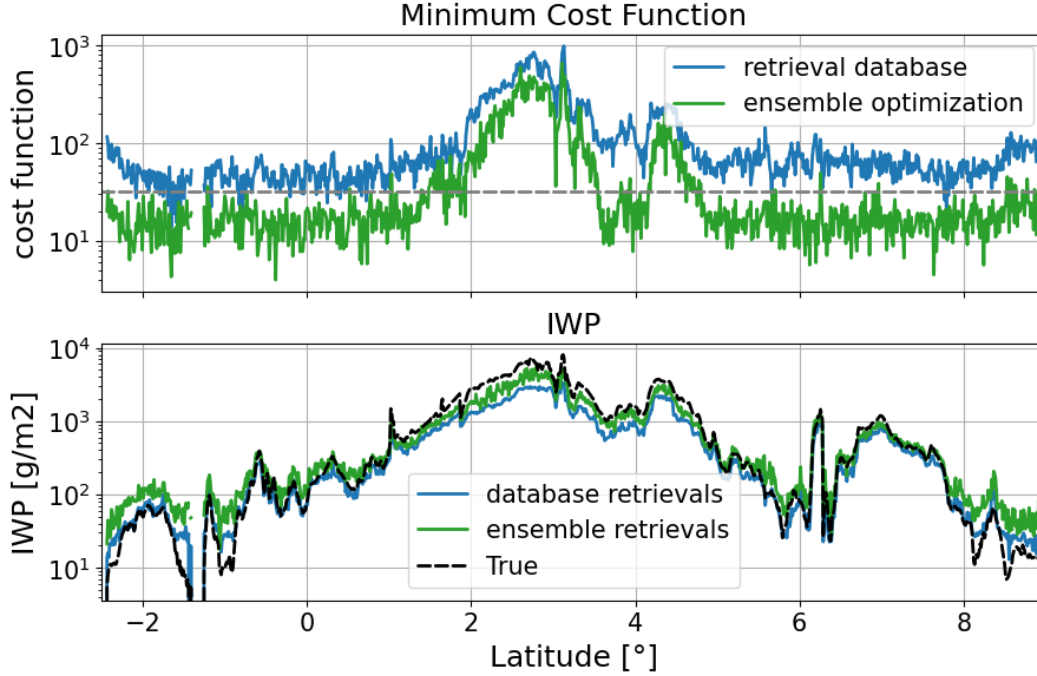


Figure 10. The top panel shows the comparison of the minimum 2 values that exist in the a priori database and in the last ensemble after optimization for the given brightness temperature observations. The bottom panel shows the comparison of the retrieved ice water path (IWP) before and after the ensemble estimation optimization.

504 for IWC, NC, and IWP are shown in different columns, and the plots for passive-only,
 505 active-only, and combined retrievals are shown in different rows. Starting from the IWC
 506 retrievals in the first column, the passive-only retrievals show the largest deviations from
 507 the diagonal line, which is not surprising since the BT measurements have low sensitiv-
 508 ity to the vertical distribution of the ice cloud microphysics. The radar-only retrievals
 509 provide much more accurate results. The scatter of points lies along the diagonal and
 510 the associated deviations are small. The radar-only retrievals are observed to bias high
 511 for the tenuous cases and bias low when IWC values are high. The reason for the low-
 512 end biases is that the radar reflectivity drops below the specified radar sensitivity, and
 513 the biases at the high end are due to non-Rayleigh effects and attenuation. The com-
 514 bined retrievals correct the high-end offset, and the scatter plots lie more along the di-
 515 agonal. The deviations of the combined retrievals are observed to become large. This
 516 is because the BT measurements are added through an ensemble approach, which gen-
 517 erates random cases over a large possible range to statistically explore the state vector
 518 space. For the NC retrievals in the second column, the passive-only retrievals again show
 519 very little skill. The NC results from the radar-only retrievals do not follow the true val-
 520 ues well. The retrieved values are always located in the range of $10^4 m^{-3}$ to $10^5 m^{-3}$,
 521 although the true values vary in a much wider range. The combined retrievals improve
 522 the NC accuracies a little, but the overall performance is still poor. The IWP retrievals
 523 show very good performance overall. All retrieved values in different panels follow the
 524 true values with small associated deviations. The IWP results from passive-only tend
 525 to underestimate the true values when IWP is small and overestimate the true values
 526 when IWP is large. The overestimation performance could possibly be corrected if more
 527 random atmospheric/cloud profiles covering the large IWP range are included in the pre-
 528 calculated radiometer retrieval database. The active-only retrievals show a similar ten-

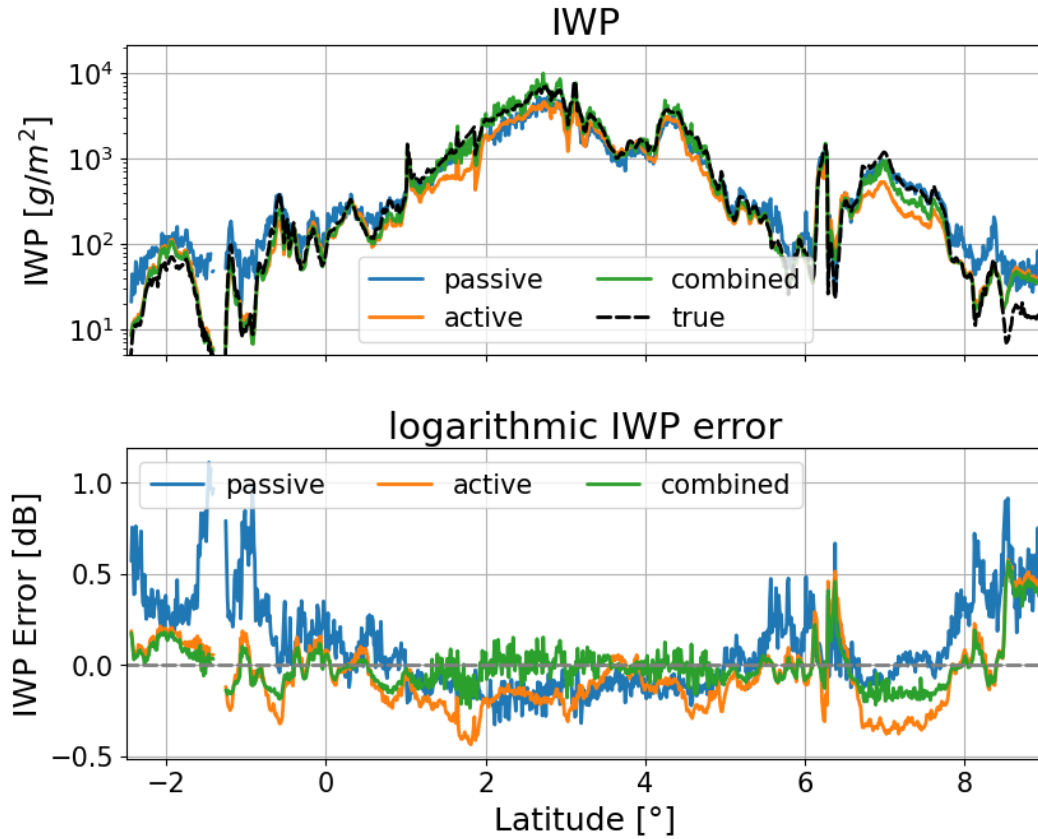


Figure 11. The top panel shows direct comparison between the retrieved ice water path (IWP) and the true values along the latitudinal transect. The passive-only, radar-only, and combined retrievals are all displayed. The bottom panel shows the logarithmic errors for different retrievals to make the comparisons clearer.

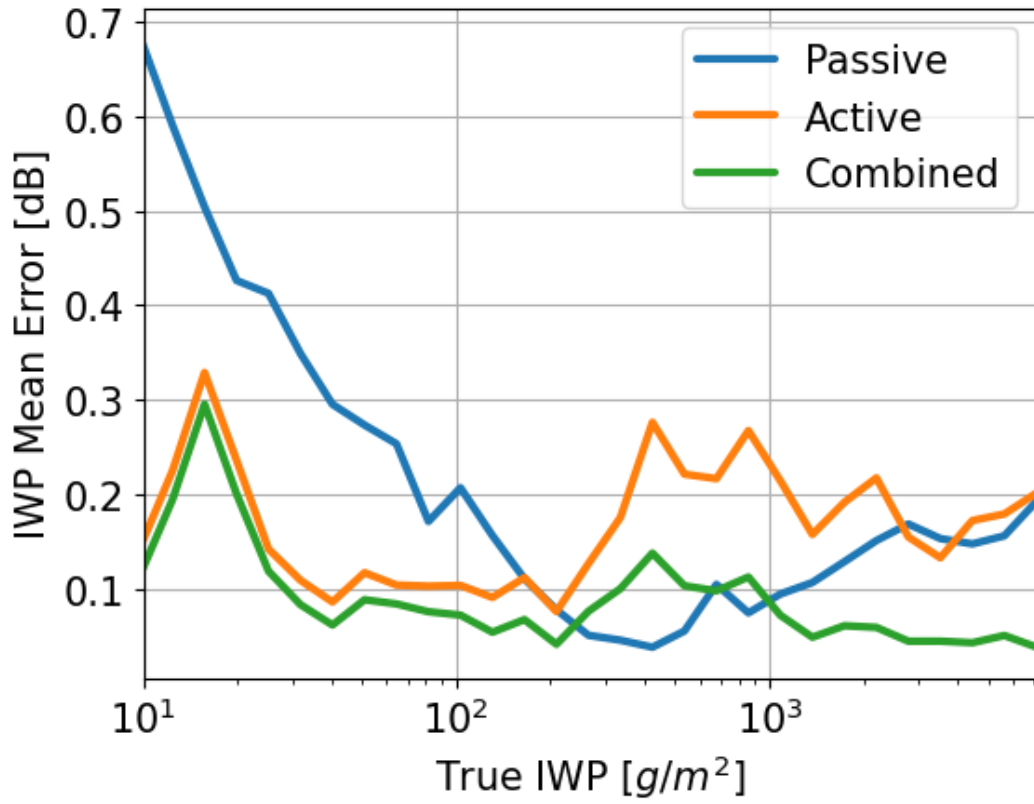


Figure 12. The mean ice water path (IWP) absolute logarithmic error in each IWP increment as a function of IWP for different retrievals.

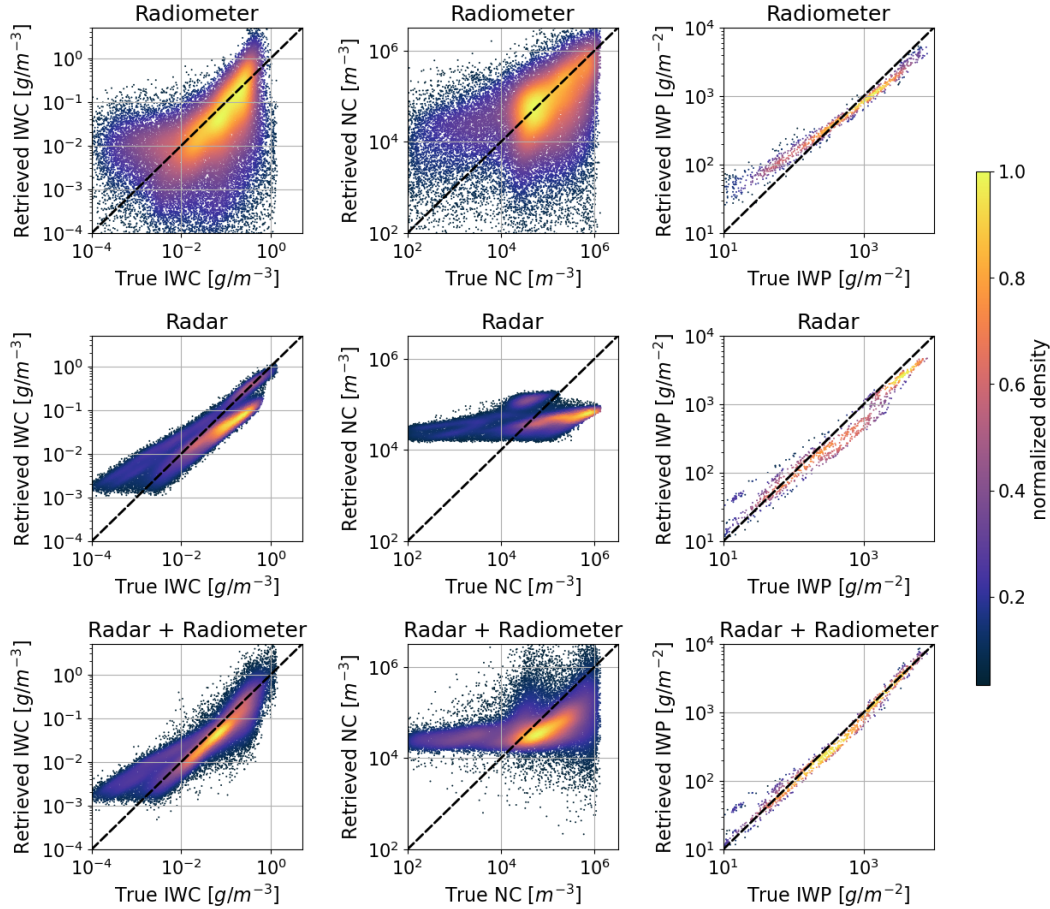


Figure 13. The scatterplots of the retrieved parameters against the true values that are colored by density. The scatterplots for ice water content (IWC), number concentration (NC), and ice water path (IWP) are shown in different columns, and the plots for passive-only, active-only, and combined retrievals are shown in different rows.

529 density, and significant improvements could be seen for the results from the combined re-
 530 retrievals.

531 Figure 14 displays the PDF of the logarithmic errors for different parameters under
 532 different retrieval methods to more quantitatively assess the retrieval performance. As
 533 displayed in the left panel, the IWC logarithmic errors for radiometer-only retrievals cover
 534 a large range from -4 dB to 2 dB, and the radar-only and combined retrievals are mostly
 535 concentrated between -1 dB to 1 dB. Compared to the error PDF for radar-only retrievals,
 536 the PDF for the synergistic retrievals has a smaller offset and smaller variance, even though
 537 the improvements are not substantial. The NC retrievals displayed in the middle panel
 538 show little skill with the logarithmic error spreading from -2.5 dB to 2.5 dB. As for the
 539 IWP retrieval displayed in the right panel, the passive-only and active-only retrievals show
 540 comparable errors, both distributing between -0.5 dB to 0.5 dB, and significant improve-
 541 ments for the synergistic retrievals is evident. Figure 15 shows the quantitative statis-
 542 tics of the absolute logarithmic error to summarize the PDF information. The left panel
 543 shows the commonly used root-mean-square deviation (RMSD) for different parameters.
 544 Since the RMSD is easily skewed by a few poor retrievals, the median errors that sep-

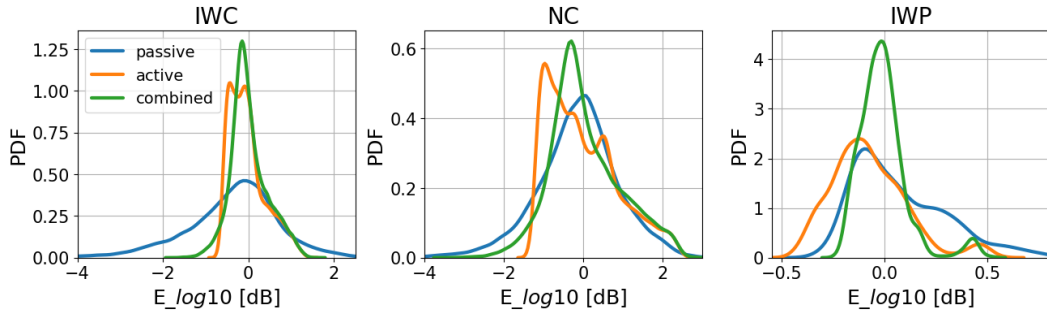


Figure 14. The probability density function (PDF) of the logarithmic errors for different ice cloud parameters under different retrieval methods.

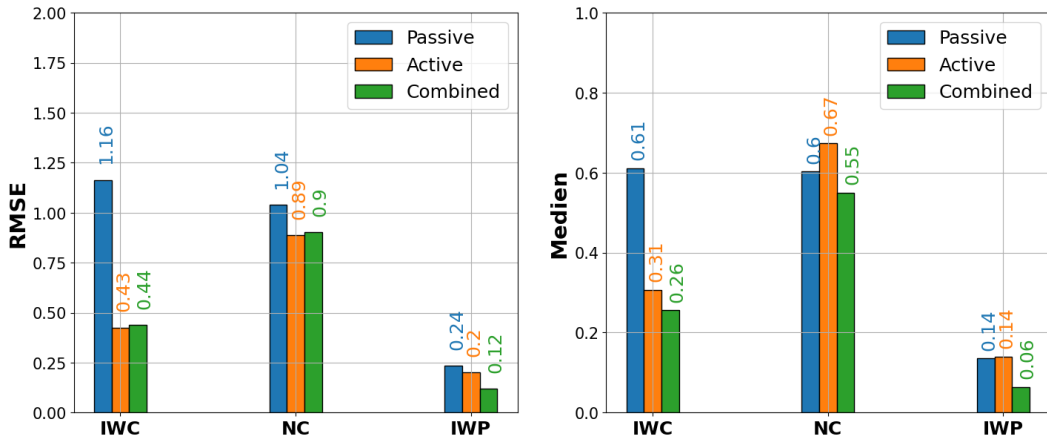


Figure 15. The quantitative statistics of the absolute logarithmic error for the retrieved ice cloud quantities. The left panel shows the root-mean-square deviation (RMSD), and the right panels show the median errors that separate the higher half from the lower half in all the retrieval error estimations.

545 arate the higher half from the lower half in all the retrieval error estimations are displayed
 546 in the right panel.

547 **6 Summaries**

548 In this study we develop a suite of hybrid Bayesian retrieval algorithms for millimeter-
 549 wave radar and submillimeter-wave radiometer to assess the ACCP observing system ca-
 550 pability in sensing ice cloud microphysical quantities. The geophysical variables we in-
 551 vestigate include the IWC, NC, and IWP. The hybrid Bayesian algorithms combine the
 552 Bayesian MCI and optimization processes to compute retrieval quantities and associated
 553 uncertainties. The radar-only retrievals employ the OEM optimization algorithm that
 554 uses gradient information to minimize the cost function. The OEM is initialized by a state
 555 vector that is constructed by implementing Bayesian MCI to each reflectivity value in
 556 different layers using the precalculated radar database. The necessary Jacobian matrix
 557 is calculated by perturbing the ice cloud microphysical quantities in different layers. The
 558 radiometer-involved retrievals employ ensemble strategies to optimize the ill-posed prob-
 559 lem. The synergistic radar and radiometer retrievals are done by generating random cases
 560 from the radar OEM results based on the Cholesky decomposition technique. The BT

561 simulations are then computed, and the Bayesian MCI is implemented to derive the fi-
 562 nal retrieval results. For the radiometer-only retrievals, the ensemble estimation algo-
 563 rithm is applied to statistically estimate the posterior pdf using the promising weighted
 564 cases. The estimation module and the sampling module proceed iteratively to stochas-
 565 tically explore the state vector space. In addition, a new approach to implement prior
 566 constrain that allow the a priori PDF to be highly non-Gaussian is proposed to make
 567 the ensemble algorithm more applicable.

568 We conducted simulation experiments to evaluate the accuracy of retrieving ice cloud
 569 quantities for different remote sensors. The simulated noisy observations are input to the
 570 hybrid Bayesian algorithms, and the retrieved parameters are compared to the known
 571 values to determine the retrieval accuracies. A tropical transect of cloud profiles that are
 572 simulated using the ECCO model is selected as the reference cloud scenes. This choice
 573 ensures the independence between the atmospheric/cloud profiles for testing and the ver-
 574 tical profiles in the a priori database. The retrieval of NC remains poor across the var-
 575 ious methods. We speculate that the addition of an observational constraint such as li-
 576 dar or visible reflectance will be needed to address NC. This will be the topic of future
 577 work. Also, we find that the radiometer observations provide little vertical information
 578 on IWC. The radar-only retrievals demonstrate skill in retrieving the IWC although the
 579 radar-only IWC retrieval biases high for tenuous volumes where the radar reflectivity drops
 580 below the sensitivity of the radar. At the high end, the radar-only IWC retrieval biases
 581 low due to non Rayleigh effects and attenuation. In future work, we will explore the skill
 582 added by lidar at the low end and lower frequency radar channels at the high end. The
 583 synergistic radar and radiometer retrievals provide significant improvements in IWP.

584 This paper provides an end-to-end idealized simulation experiment that sacrifices
 585 precise reality in order to demonstrate nuances in the various algorithms. Several dis-
 586 advantages are worth mentioning. Firstly, the reference cloud scenes only contain frozen
 587 hydrometers, and the retrieval performance under more complex atmospheric scenarios
 588 is not investigated. Also, the forward model in this study only applies the EvansSnow
 589 particle habit, and the uncertainties caused by various particle habits are not considered.
 590 Secondly, the statistical characteristics are only derived based on selected atmospheric/cloud
 591 profiles along a latitudinal transect. Since this subset with a finite number of profiles can
 592 hardly represent the realistic spatial distribution of ice cloud microphysics, the statis-
 593 tics we derive may differ from the characteristics of the entire possible atmospheric con-
 594 ditions. Thirdly, apart from the W-band radar and the submillimeter-wave radiometer,
 595 the ACCP observing system includes other remote sensors that would be highly help-
 596 ful to improve retrieval accuracies for ice cloud remote sensing. For instance, highly ac-
 597 curate Doppler velocity measurements may allow for constraints on the ice crystal bulk
 598 density that could significantly mitigate forward model uncertainties. The retrieval per-
 599 formance by combining other synergistic information content remains to be investigated.

600 **Acknowledgments**

601 This research was supported by NASA Grants NNX15AK17G and 80NSSC19K1087 both
 602 administered from the Goddard Space Flight Center under the NASA ACE and ACCP
 603 programs, respectively. We thank for Prof. Pavlos Kollias at Stony Brook University for
 604 providing the atmospheric scenes from the ECCO model that we used for evaluating the
 605 synergistic retrievals. The TC4 in situ data for this study were collected by the mem-
 606 bers of the Stratton Park Engineering Corporation led by Paul Lawson, as well as An-
 607 drew Heymsfield at the National Center for Atmospheric Research. The CloudSat data
 608 were obtained from the CloudSat Data Processing Center at the Colorado State Univer-
 609 sity's Cooperative Institute for Research in the Atmosphere (CIRA). All TC4 data are
 610 publicly and freely available in the NASA data archive at <https://espoarchive.nasa.gov/archive/browse/tc4>,
 611 and the CloudSat data are available at <http://www.cloudsat.cira.colostate.edu/data-products>.

612

References

613

Ackerman, T., Liou, K., Valero, F., & Pfister, L. (1988). Heating rates in tropical anvils. *Journal of the atmospheric sciences*, *45*(10), 1606–1623.

614

615

Berry, E., & Mace, G. (2014). Cloud properties and radiative effects of the asian summer monsoon derived from atrain data. *Journal of Geophysical Research: Atmospheres*, *119*(15), 9492–9508.

616

617

618

Board, S., National Academies of Sciences, E., & Medicine. (2019). Thriving on our changing planet: A decadal strategy for earth observation from space. *National Academies Press*.

619

620

621

Brath, M., Ekelund, R., Eriksson, P., Lemke, O., & Buehler, S. (2020). Microwave and submillimeter wave scattering of oriented ice particles. *Atmospheric Measurement Techniques*, *13*(5), 2309–2333.

622

623

624

Brath, M., Fox, S., Eriksson, P., Harlow, R., Burgdorf, M., & Buehler, S. (2018). Retrieval of an ice water path over the ocean from ismar and marss millimeter and submillimeter brightness temperatures. *Atmospheric Measurement Techniques*, *11*(1), 611–632.

625

626

627

Buehler, S., Defer, E., Evans, F., Eliasson, S., Mendrok, J., Eriksson, P., . . . Kasai, Y. (2012). Observing ice clouds in the submillimeter spectral range: the cloudice mission proposal for esa’s earth explorer 8. *Atmospheric Measurement Techniques*, *5*(7), 1529–1549.

628

629

630

Buehler, S., Eriksson, P., Kuhn, T., Von Engel, A., & Verdes, C. (2005). Arts, the atmospheric radiative transfer simulator. *Journal of Quantitative Spectroscopy and Radiative Transfer*, *91*(1), 65–93.

631

632

633

Chen, J., Pendlebury, D., Gravel, S., Stroud, C., Ivanova, I., DeGranpr, J., & Plummer, D. (2018). Development and current status of the gem-mach-global modelling system at the environment and climate change canada. *In International Technical Meeting on Air Pollution Modelling and its Application*, 107–112.

634

635

636

Cote, G. S. M. A. P. A. R. M., J., & Staniforth, A. (1998). The operational cmcmrb global environmental multiscale (gem) model. part i: Design considerations and formulation. *Monthly Weather Review*, *126*(6), 1373–1395.

637

638

639

Delanoe, J., Protat, A., Testud, J., Bouniol, D., Heymsfield, A., Bansemmer, A., . . . Forbes, R. (2005). Statistical properties of the normalized ice particle size distribution. *Journal of Geophysical Research: Atmospheres*, *110*(D10).

640

641

642

Eriksson, P., Buehler, S., Davis, C., Emde, C., & Lemke, O. (2011). Arts, the atmospheric radiative transfer simulator, version 2. *Journal of Quantitative Spectroscopy and Radiative Transfer*, *12*(10), 1551–1558.

643

644

645

Eriksson, P., Ekelund, R., Mendrok, J., Brath, M., Lemke, O., & Buehler, S. (2018). A general database of hydrometeor single scattering properties at microwave and sub-millimetre wavelengths. *Earth System Science Data*, *10*(3), 1301–1326.

646

647

648

Eriksson, P., Rydberg, B., Mattioli, V., Thoss, A., Accadia, C., Klein, U., & Buehler, S. (2020). Towards an operational ice cloud imager (ici) retrieval product. *Atmospheric Measurement Techniques*, *13*(1), 53–71.

649

650

651

Evans, K. (2007). Shdomppda: A radiative transfer model for cloudy sky data assimilation. *Journal of the atmospheric sciences*, *66*(11), 3854–3864.

652

653

654

Evans, K., Walter, S., Heymsfield, A., & McFarquhar, G. (2002). Submillimeterwave cloud ice radiometer: Simulations of retrieval algorithm performance. *Journal of Geophysical Research: Atmospheres*, *107*(D3), AAC-2.

655

656

657

Evans, K., Wang, J., Racette, P., Heymsfield, G., & Li, L. (2005). Ice cloud retrievals and analysis with the compact scanning submillimeter imaging radiometer and the cloud radar system during crystal face. *Journal of Applied Meteorology*, *44*(6), 839–859.

658

659

660

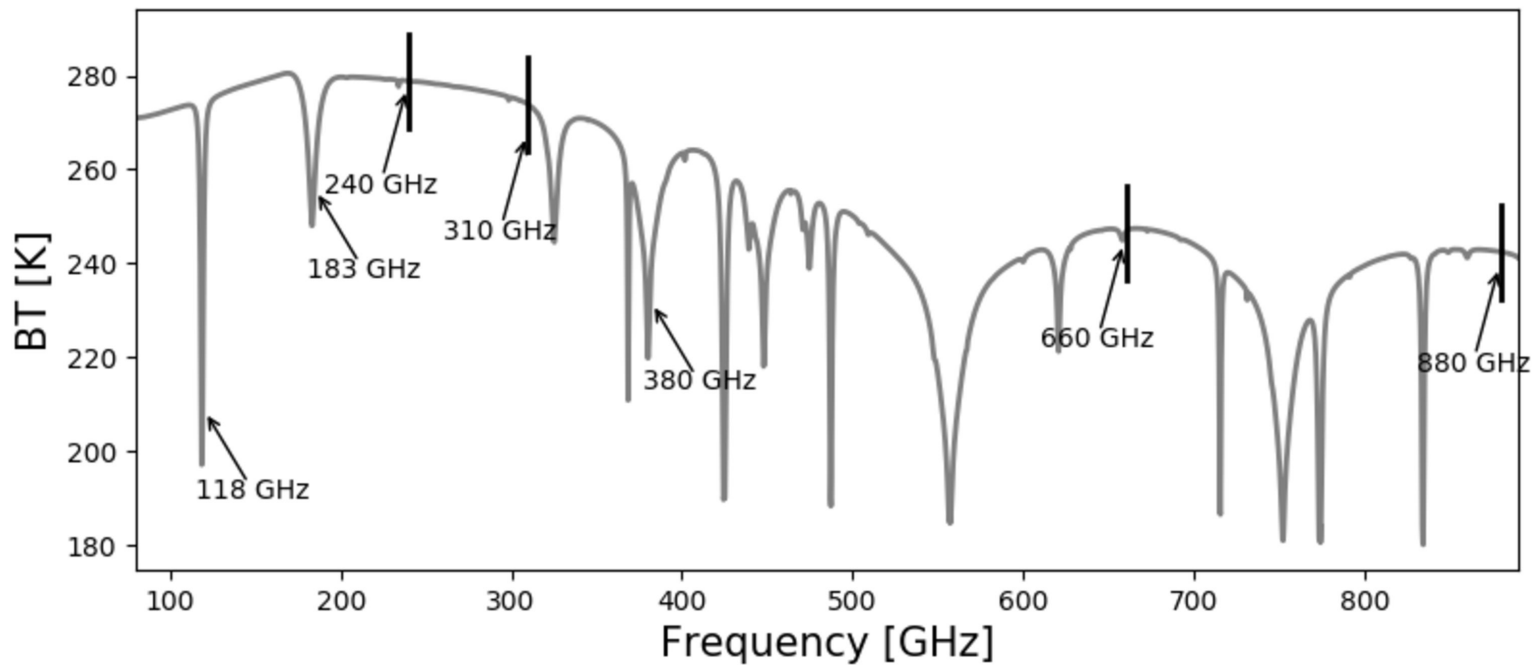
Evans, K., Wang, J., Starr, O., Heymsfield, G., Li, L., Tian, L., . . . Bansemmer, A. (2012). Ice hydrometeor profile retrieval algorithm for high-frequency

661

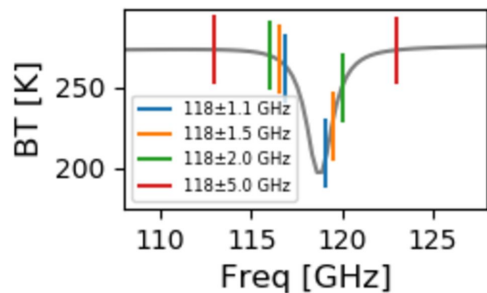
662

- microwave radiometers: application to the cossir instrument during tc4. *Atmospheric Measurement Techniques*, 5(9), 2277–2306.
- Hartmann, D., & Berry, S. (2017). The balanced radiative effect of tropical anvil clouds. *Journal of Geophysical Research: Atmospheres*, 122(9), 5003–5020.
- Jimenez, C., Buehler, S., Rydberg, B., Eriksson, P., & Evans, K. (2007). Performance simulations for a submillimetrewave satellite instrument to measure cloud ice. *Quarterly Journal of the Royal Meteorological Society: A journal of the atmospheric sciences, applied meteorology and physical oceanography*, 133(s2), 129–149.
- Kangas, V., D’Addio, S., Klein, U., Loiselet, M., Mason, G., Orhac, J., . . . Thomas, B. (2014). Performance simulations for a submillimetrewave satellite instrument to measure cloud ice. *Ice cloud imager instrument for MetOp Second Generation. In 2014 13th Specialist Meeting on Microwave Radiometry and Remote Sensing of the Environment (MicroRad)*, 228–231.
- Liu, K. (1986). Influence of cirrus clouds on weather and climate processes: A global perspective. *Monthly Weather Review*, 114(6), 1167–1199.
- Liu, Y., Buehler, S., Brath, M., Liu, H., & Dong, X. (2018). Ensemble optimization retrieval algorithm of hydrometeor profiles for the ice cloud imager submillimetrewave radiometer. *Journal of Geophysical Research: Atmospheres*, 123(9), 4594–4612.
- Liu, Y., & Mace, G. (2020). Synthesizing the vertical structure of tropical cirrus by combining cloudsat radar reflectivity with in situ microphysical measurements using bayesian monte carlo integration. *Journal of Geophysical Research: Atmospheres*, 125(18), e2019JD031882.
- Pfreundschuh, S., Eriksson, P., Buehler, S., Brath, M., Duncan, D., Larsson, R., & Ekelund, R. (2020). Synergistic radar and radiometer retrievals of ice hydrometeors. *Atmospheric Measurement Techniques*, 13(8), 4219–4245.
- Rodgers, C. (2000). Inverse methods for atmospheric sounding: theory and practice. *World scientific*.
- Stephens, G., Vane, D., Tanelli, S., Im, E., Durden, S., Rokey, M., . . . L’Ecuyer, T. (2008). Cloudsat mission: Performance and early science after the first year of operation. *Journal of Geophysical Research: Atmospheres*, 113(D8).
- Stephens, G., & Webster, P. (1984). Cloud decoupling of the surface and planetary radiative budgets. *Journal of the Atmospheric Sciences*, 41(4), 681–686.
- Su, H., Jiang, J., Neelin, J., Shen, T., Zhai, C., Yue, Q., . . . Yung, Y. (2017). Tightening of tropical ascent and high clouds key to precipitation change in a warmer climate. *Nature communications*, 8, 15771.
- Tanelli, S., Durden, S., Im, P. K., E., Reinke, D., Partain, P., Haynes, J., & Marchand, R. (2008). Cloudsat’s cloud profiling radar after two years in orbit: Performance, calibration, and processing. *IEEE Transactions on Geoscience and Remote Sensing*, 46(11), 3560–3573.
- Toon, O., Starr, D., Jensen, E., Newman, P., Platnick, S., Schoeberl, M., . . . Jucks, K. (2010). Planning, implementation, and first results of the tropical composition, cloud and climate coupling experiment (tc4). *Journal of Geophysical Research: Atmospheres*, 115(D10), 3560–3573.
- Zelinka, M., & Hartmann, D. (2011). The observed sensitivity of high clouds to mean surface temperature anomalies in the tropics. *Journal of Geophysical Research: Atmospheres*, 116(D23).

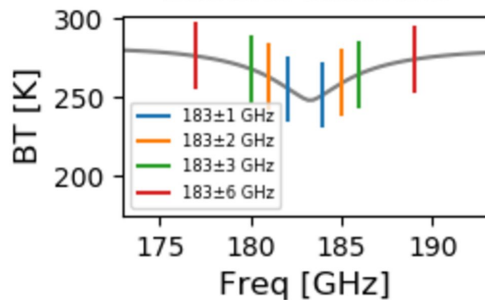
Figure1.



118GHz Channels



183GHz Channels



380GHz Channels

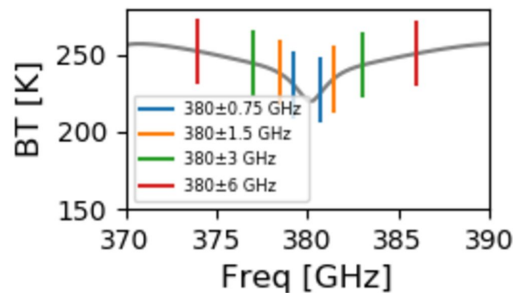
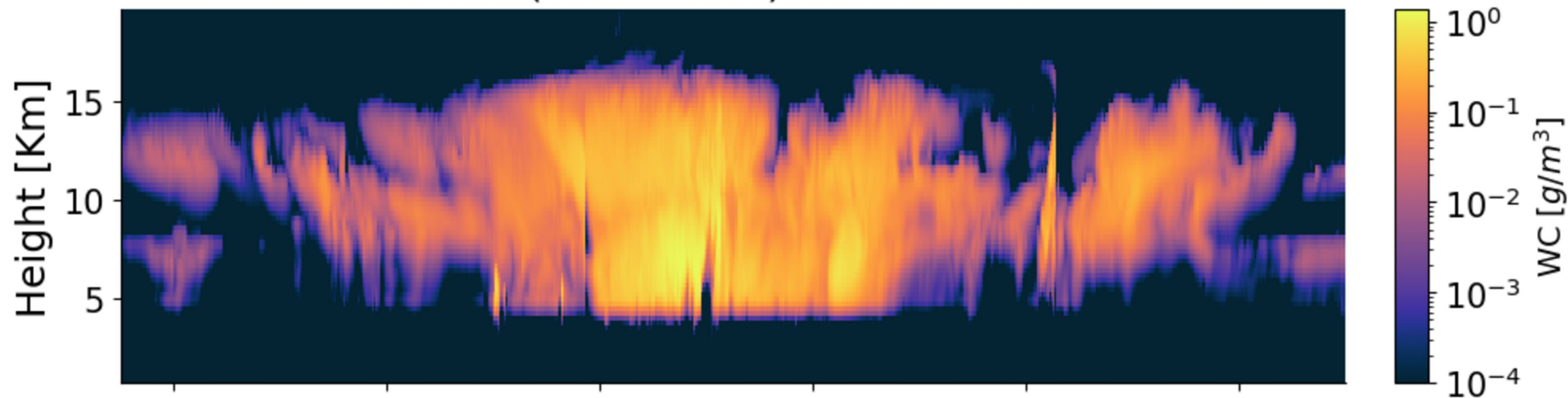
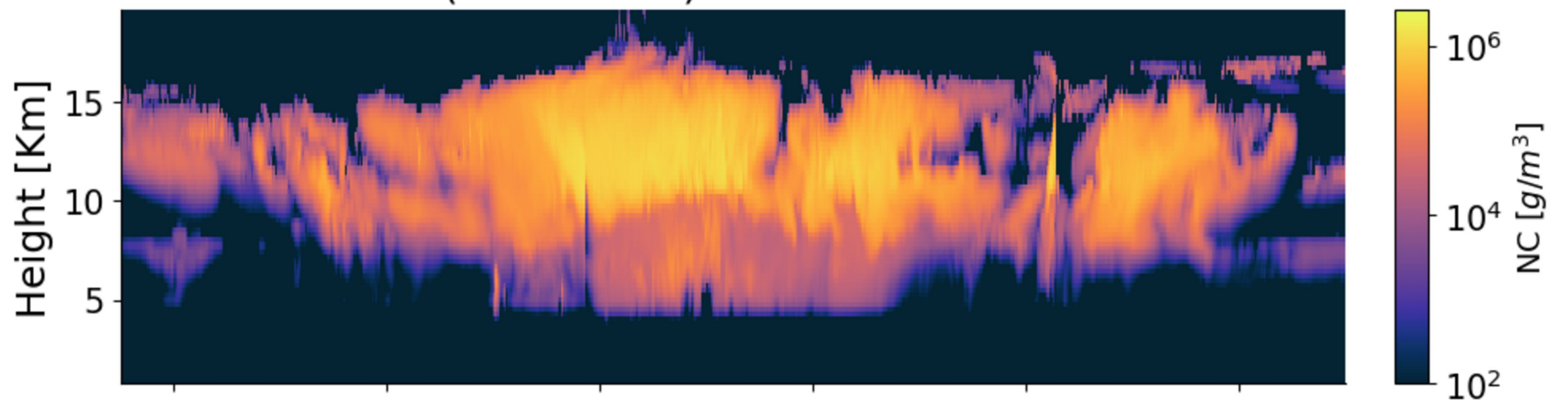


Figure2.

Frozen (Ice + Snow) Water Content



Frozen (Ice + Snow) Number Concentration



W-band Radar Simulations

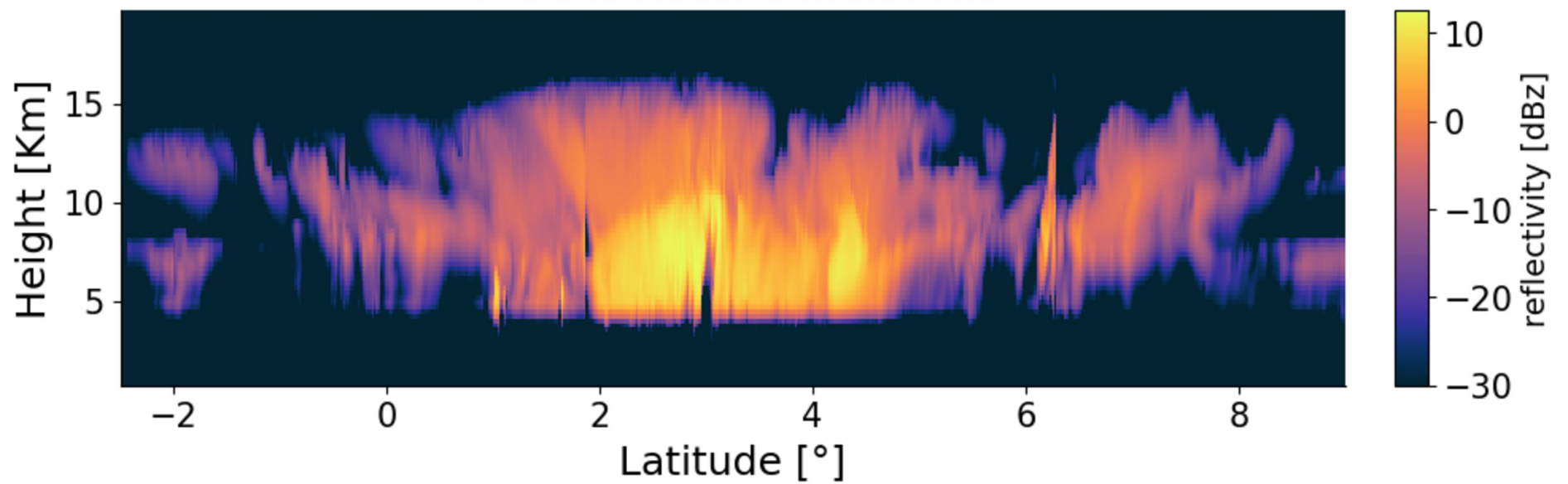
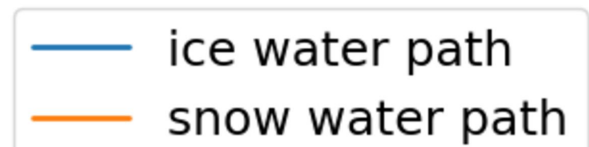
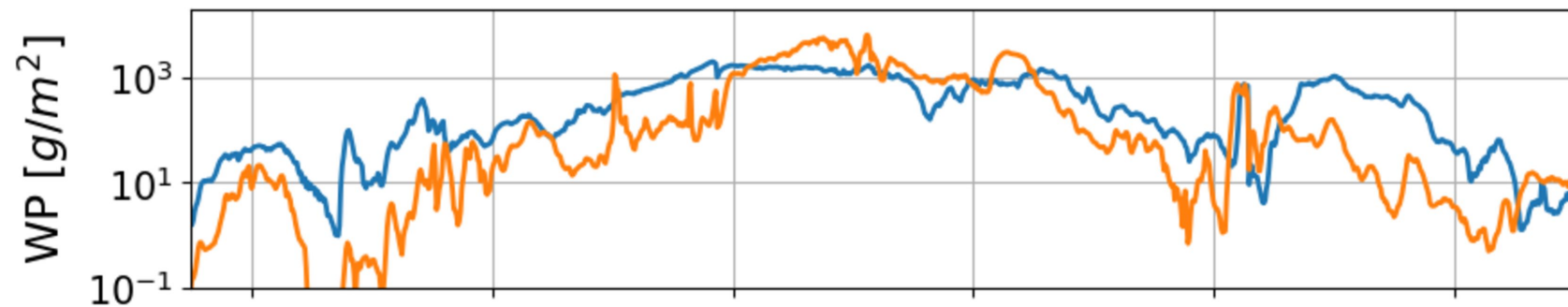
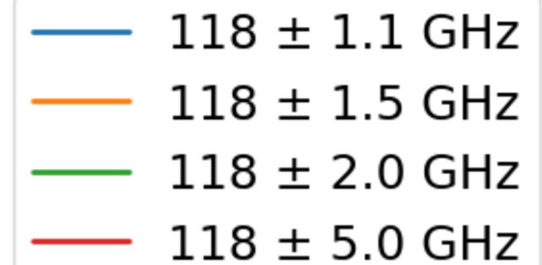
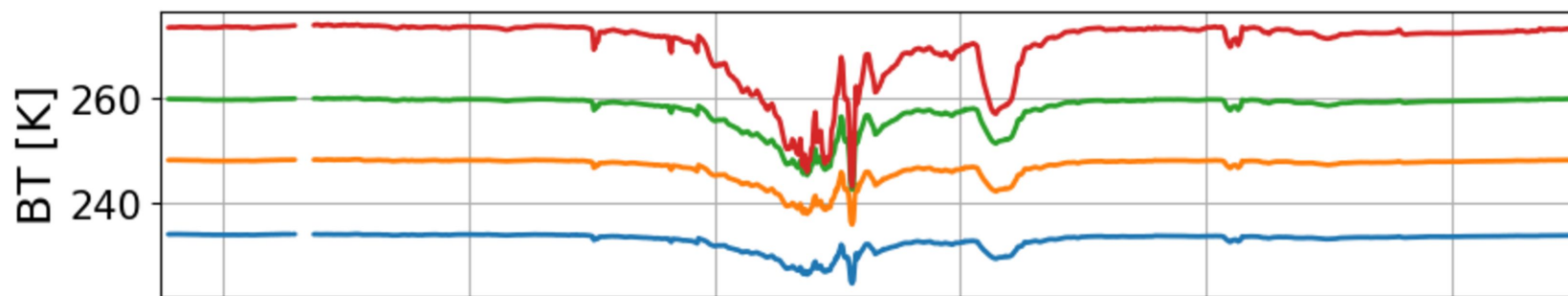


Figure3.

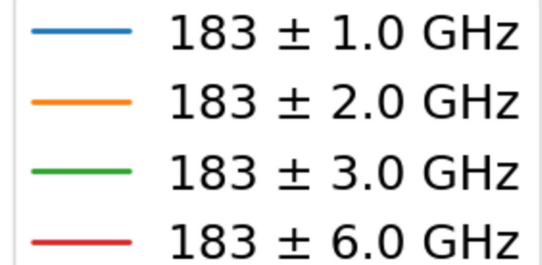
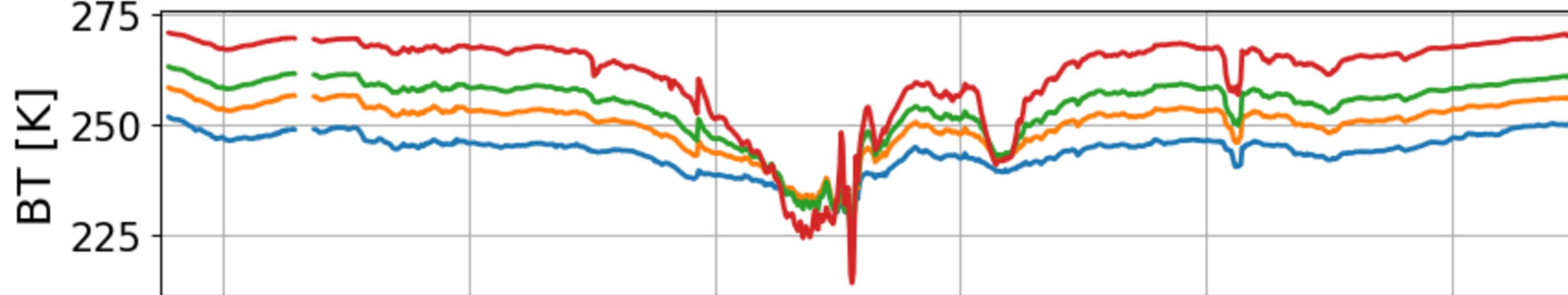
Frozen Water Path



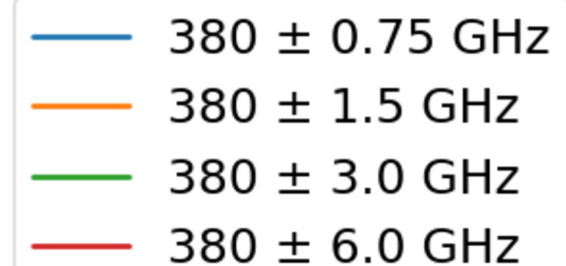
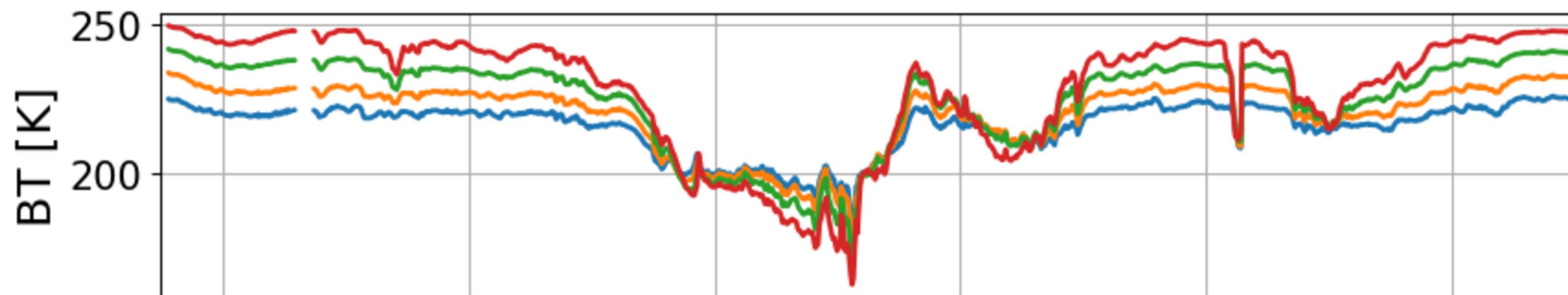
118 Ghz Channels



183 Ghz Channels



380 Ghz Channels



Window Channels

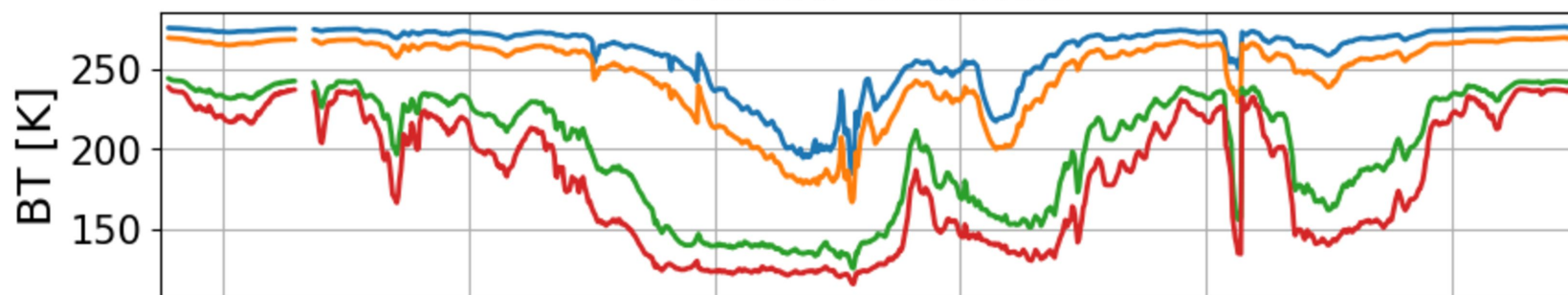
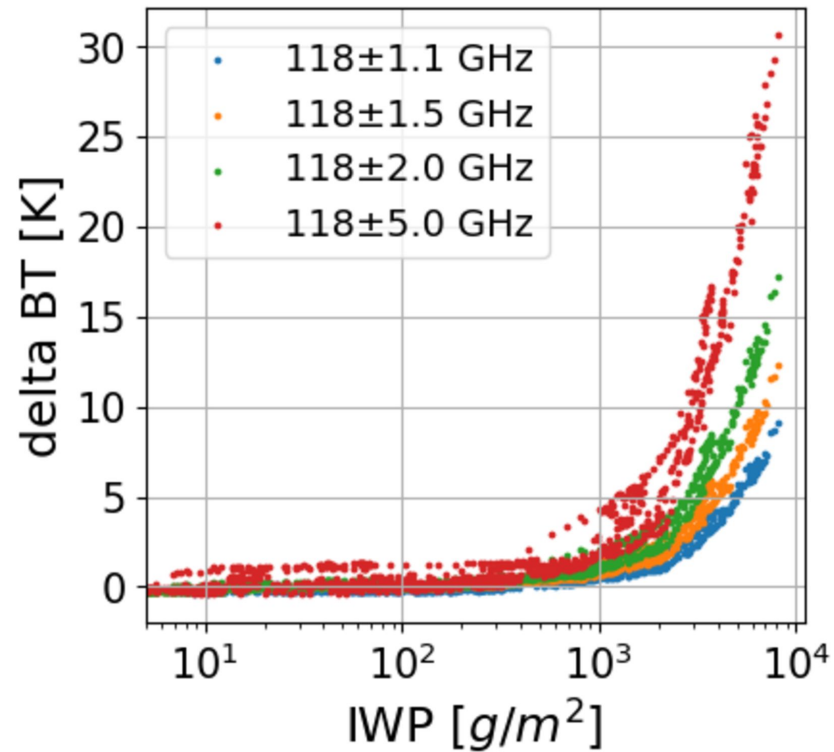
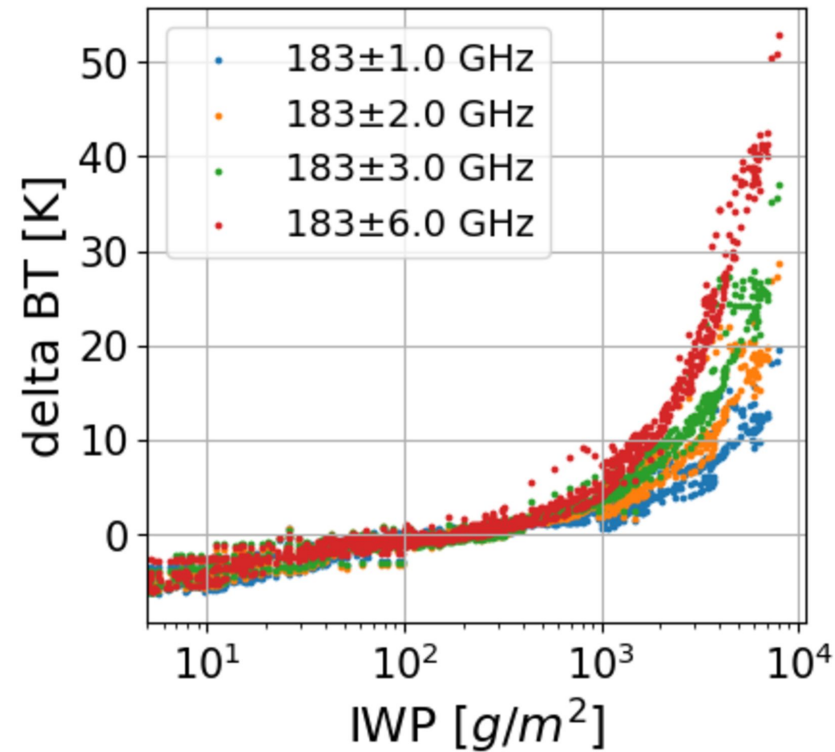
Latitude [$^\circ$]

Figure4.

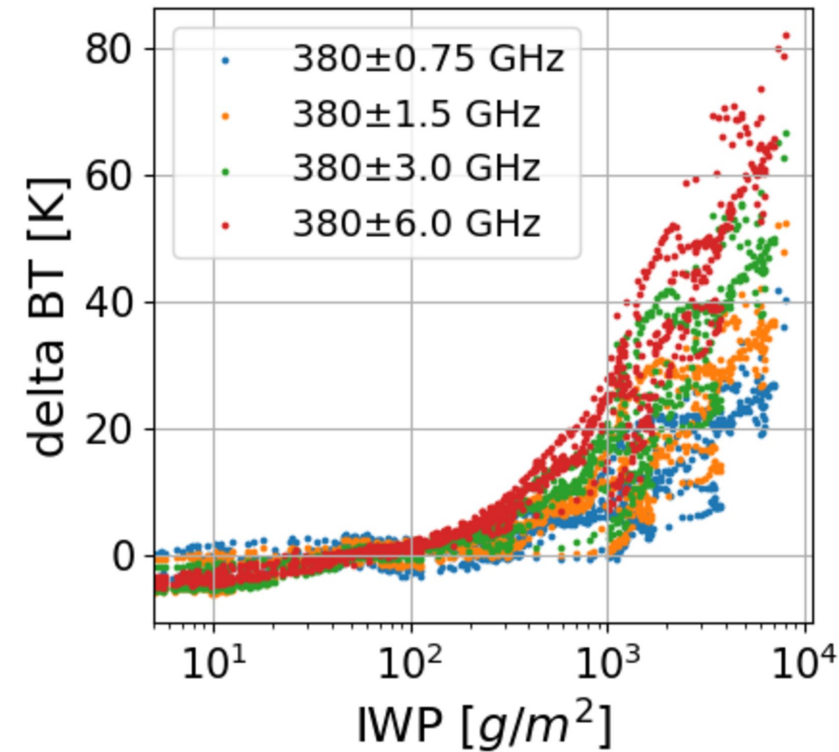
118 GHz Channels



183 GHz Channels



380 GHz Channels



Window Channels

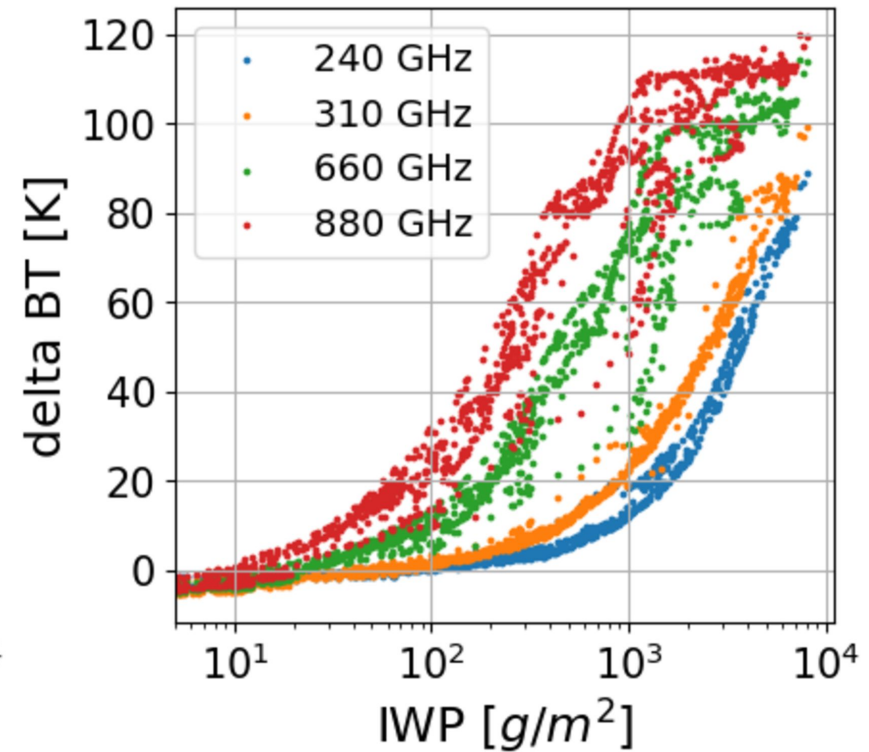


Figure 5.

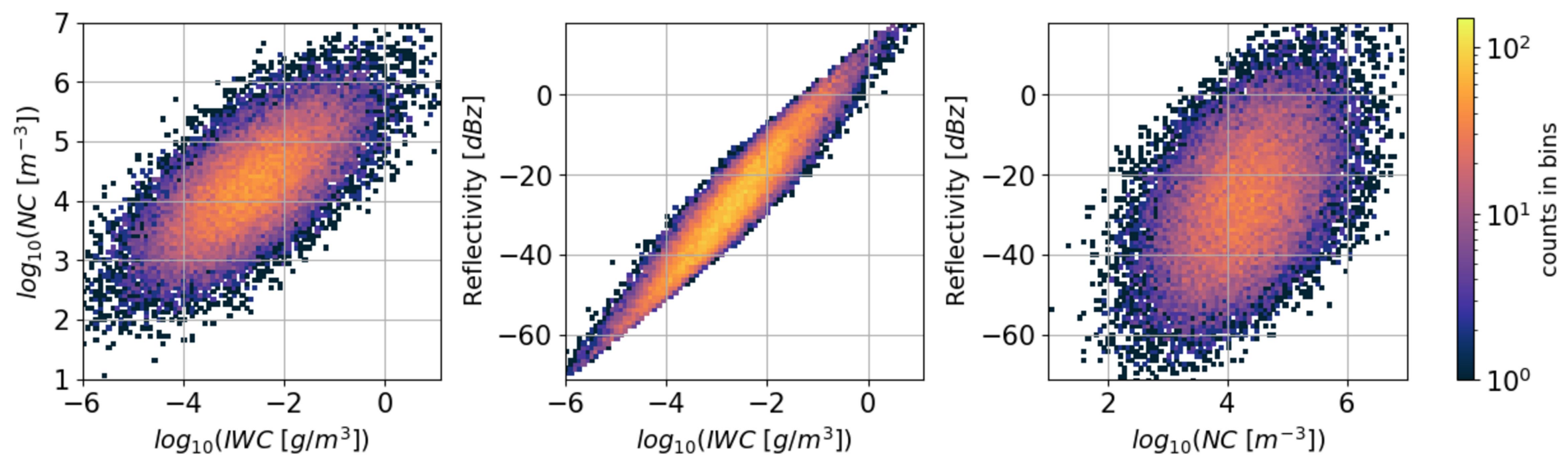


Figure6.

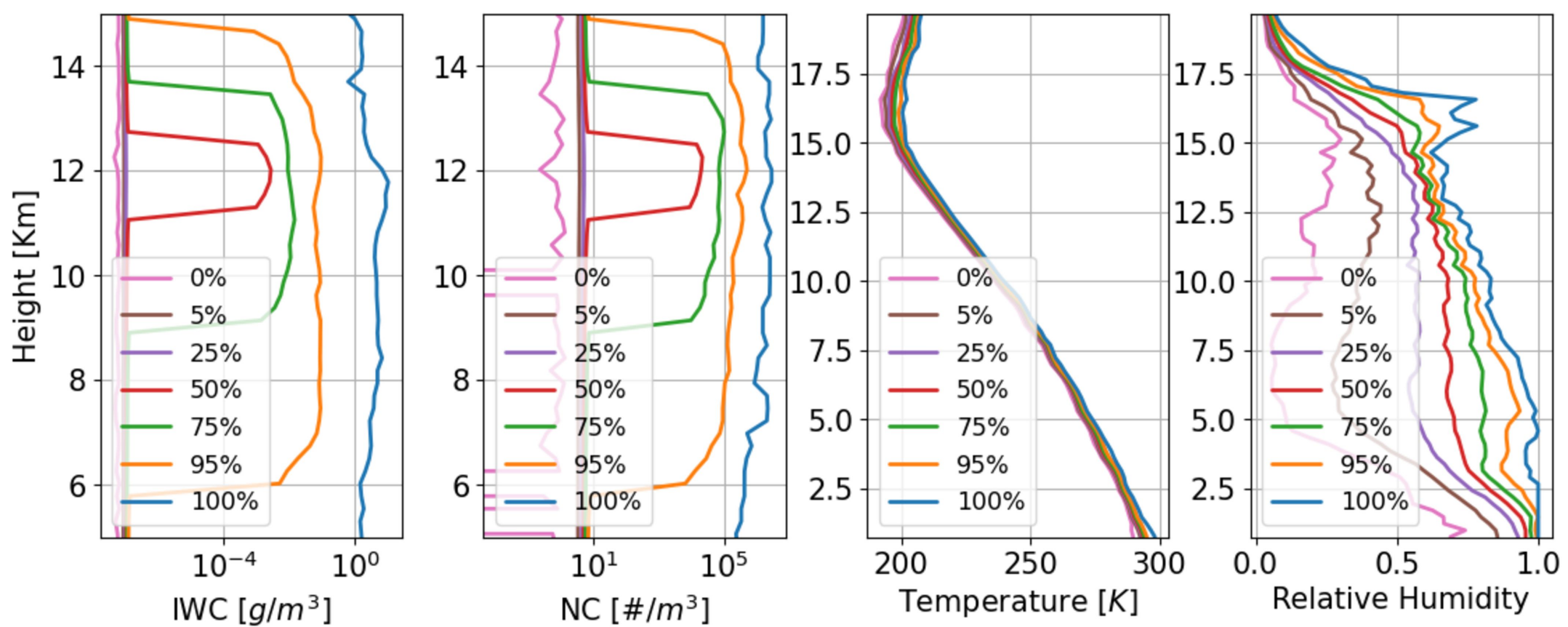


Figure 7.

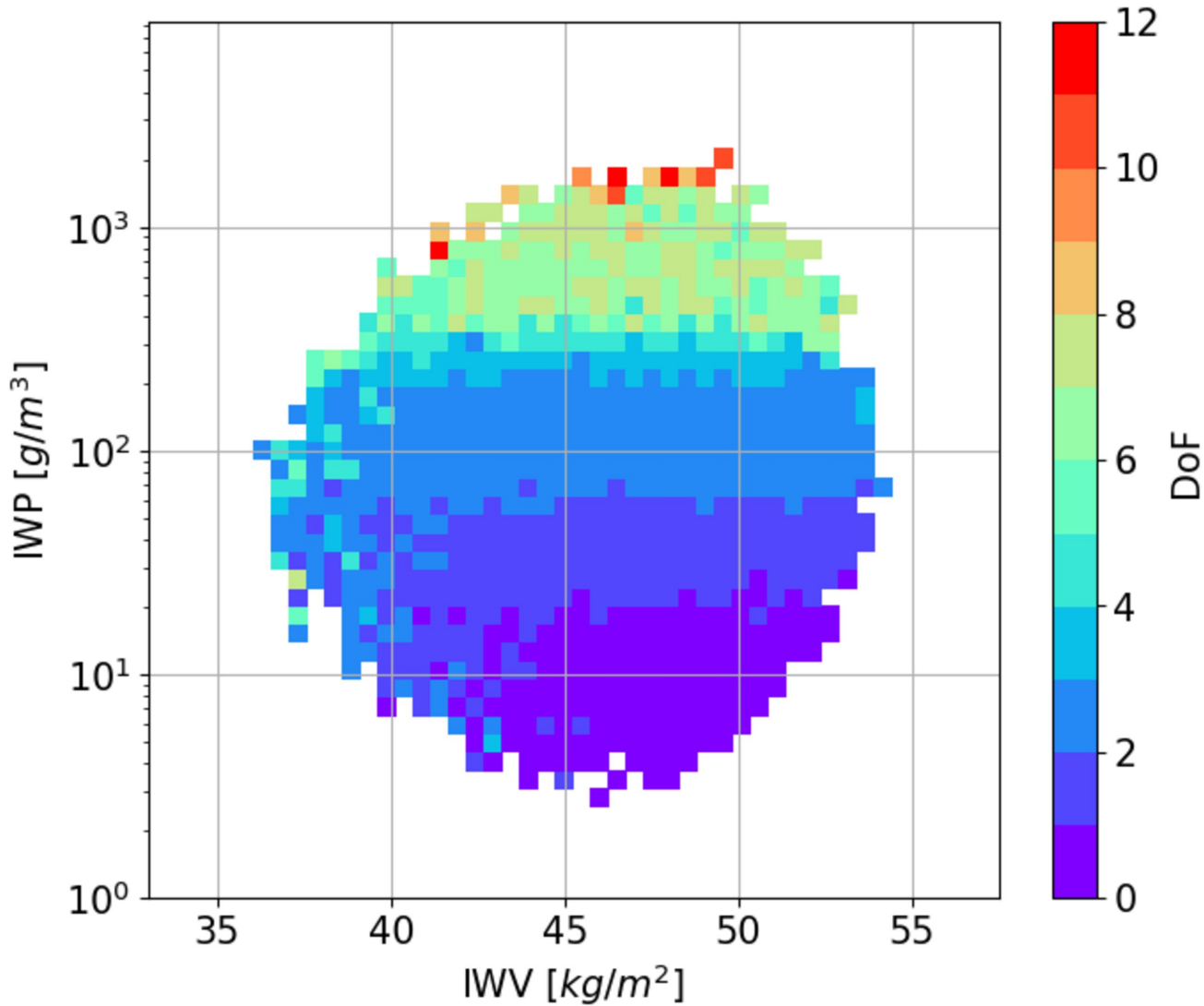
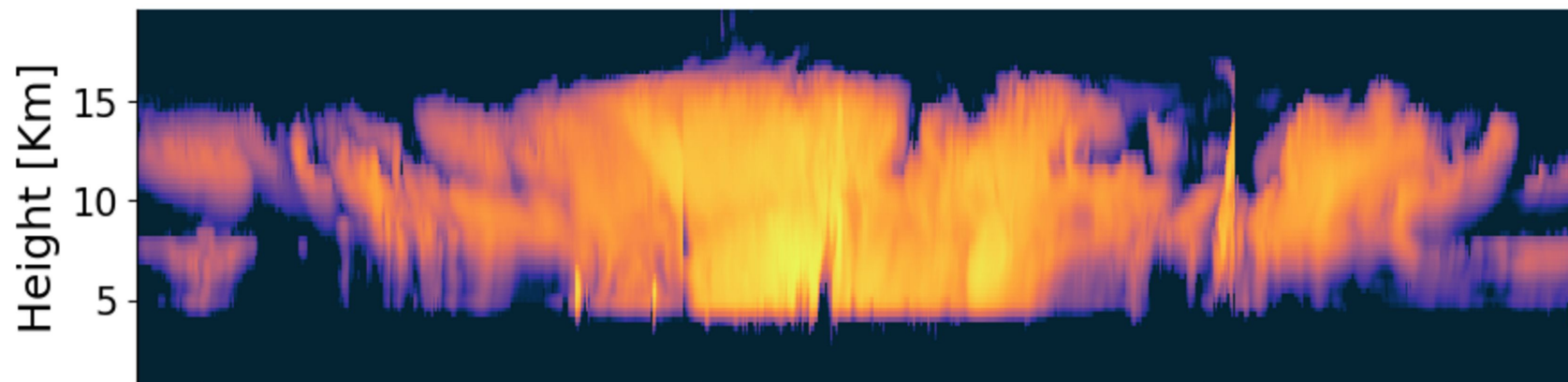
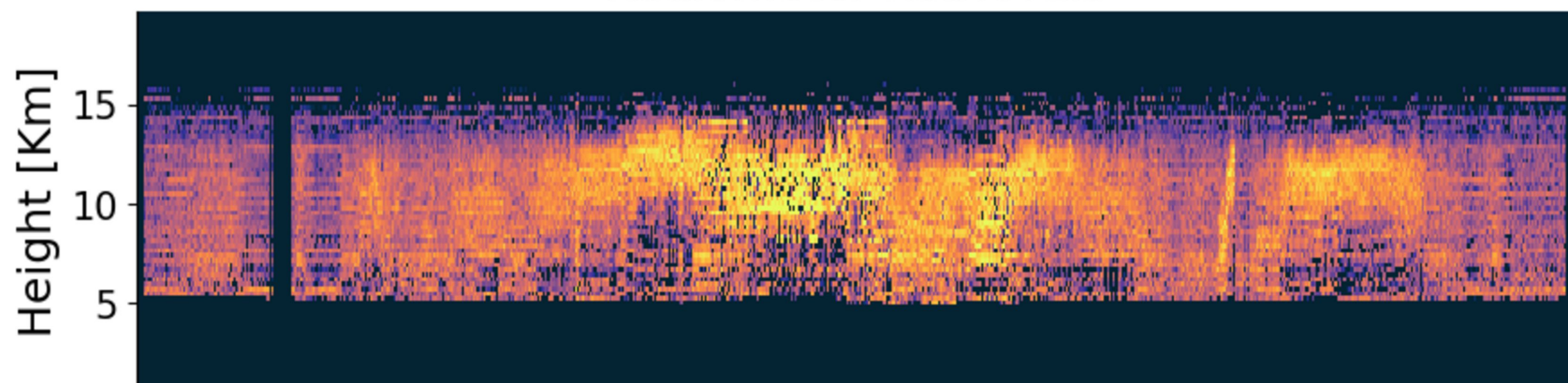


Figure 8.

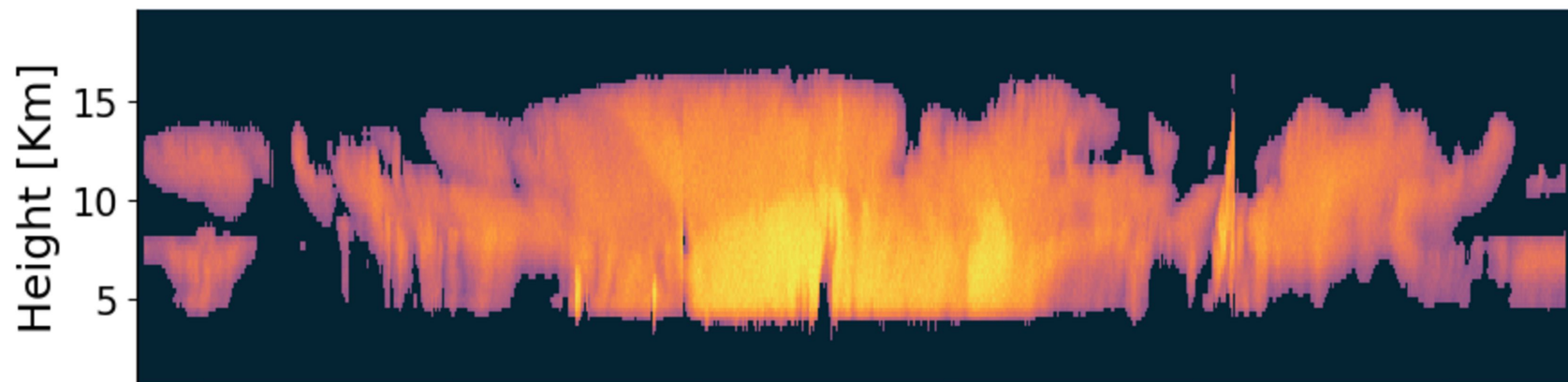
True Ice + Snow Water Content



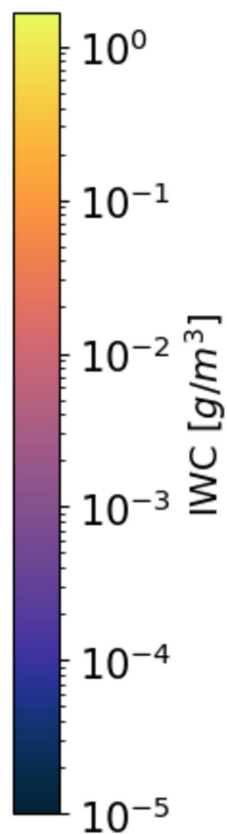
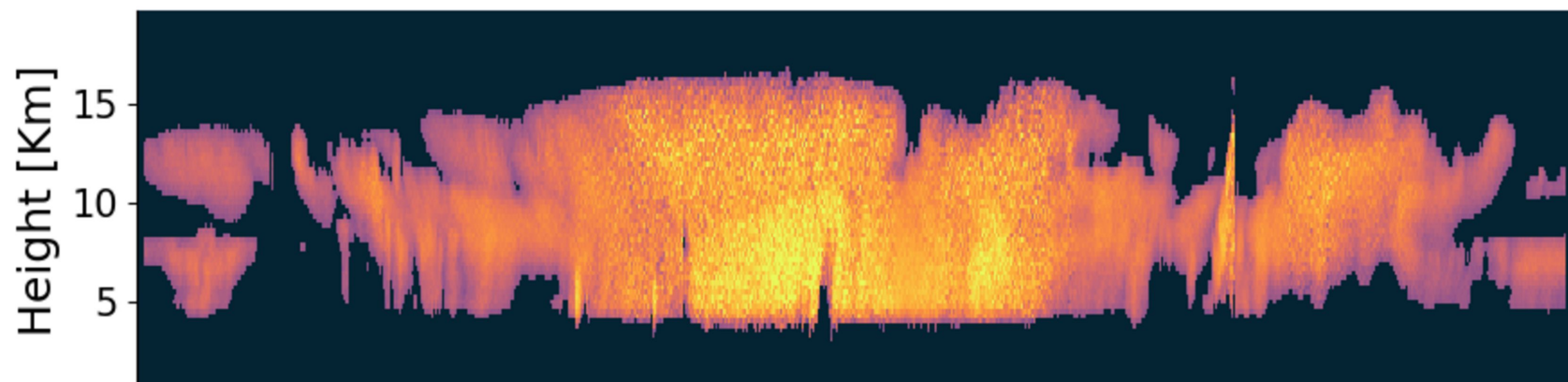
Radiometer Retrievals



Radar Retrievals



Radar + Radiometer Retrievals

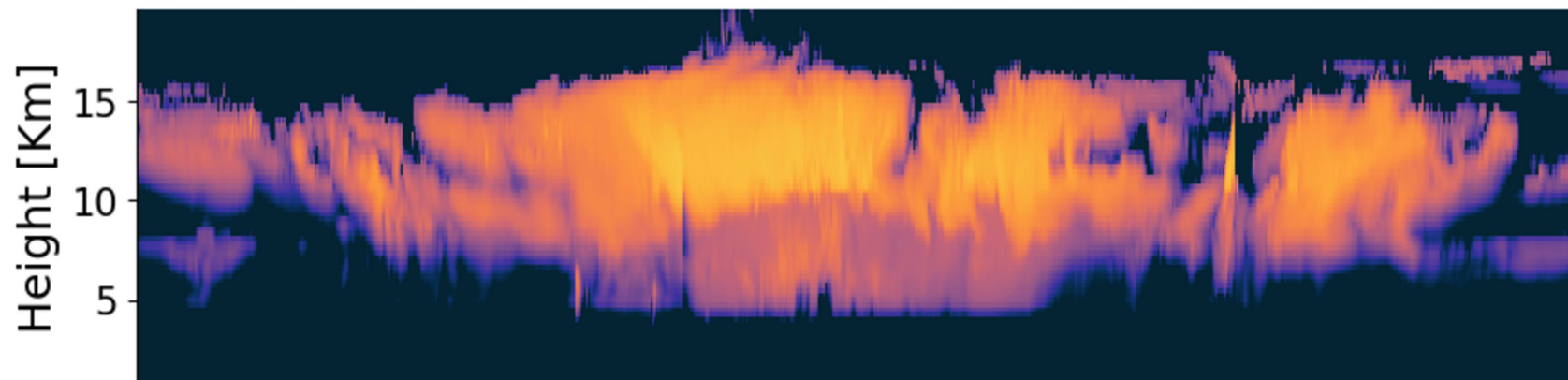


-2 0 2 4 6 8

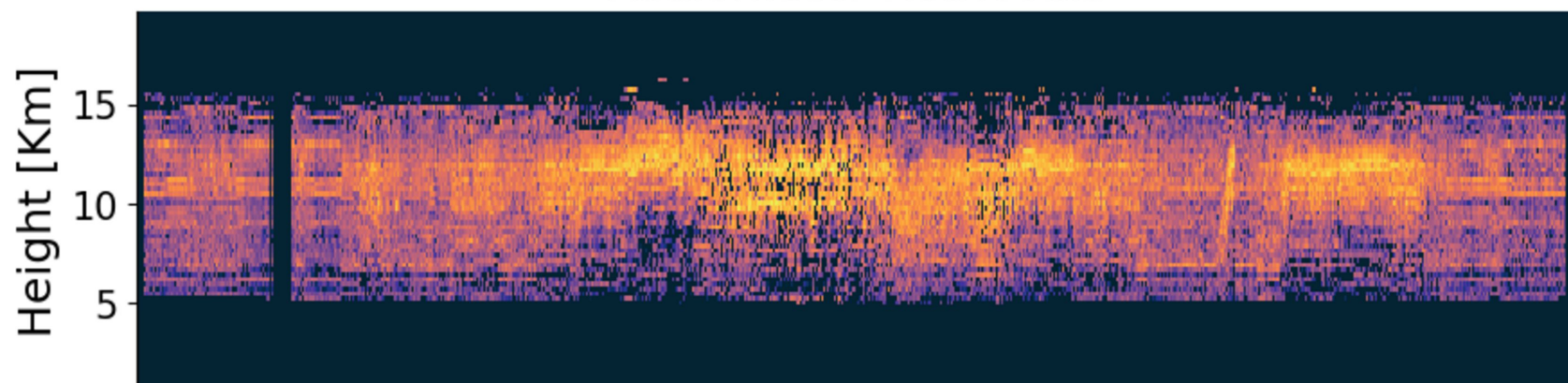
Latitude [°]

Figure9.

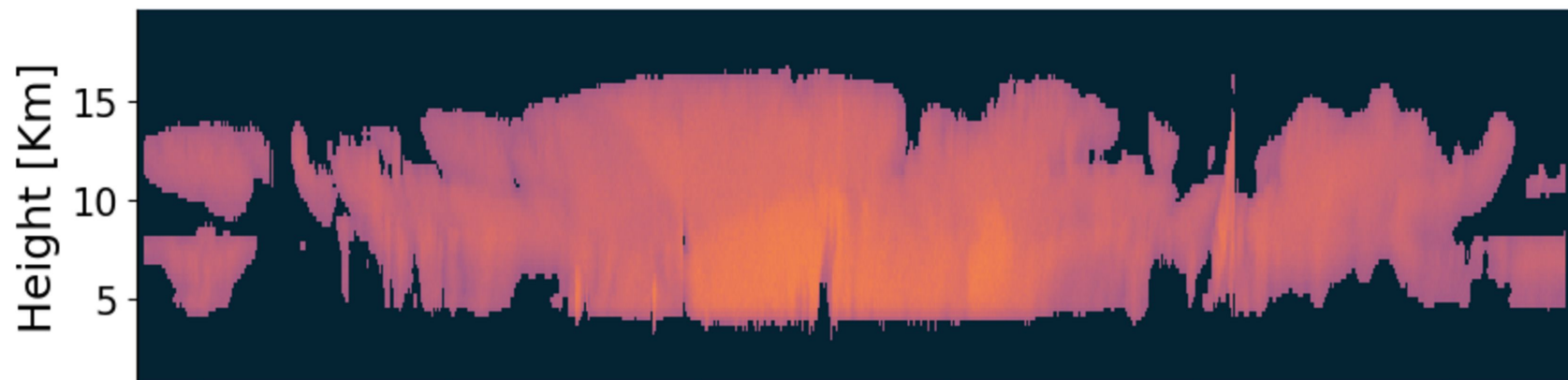
True Ice + Snow Number Concentration



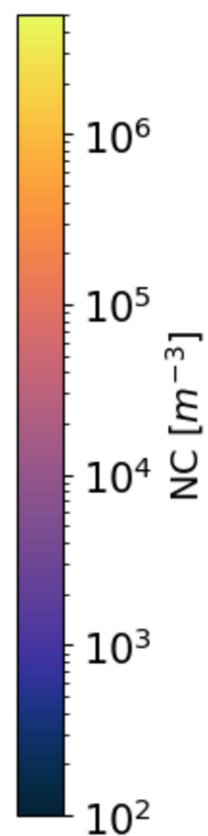
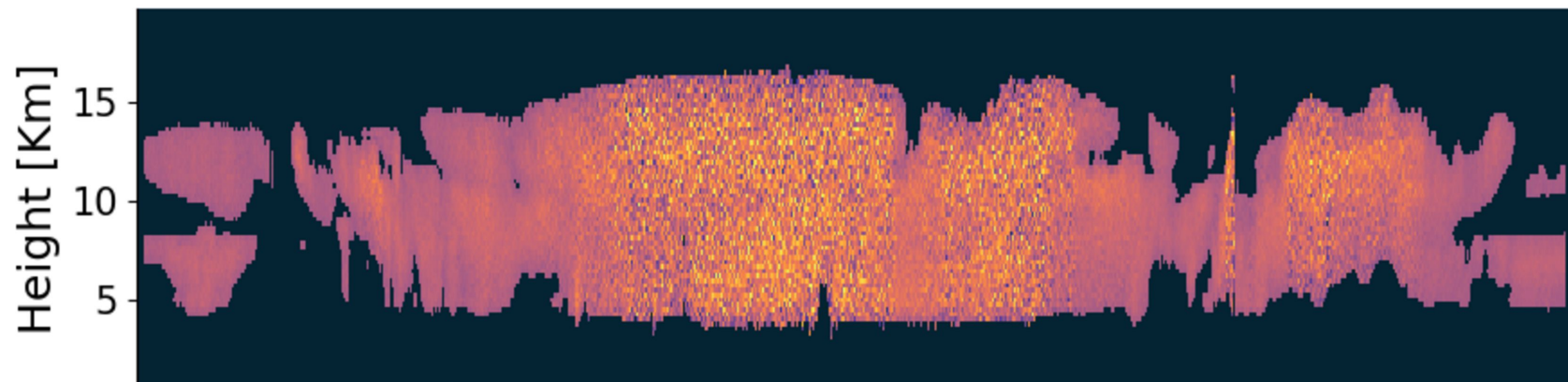
Radiometer Retrievals



Radar Retrievals



Radar + Radiometer Retrievals



-2

0

2

4

6

8

Latitude [$^{\circ}$]

Figure10.

Minimum Cost Function

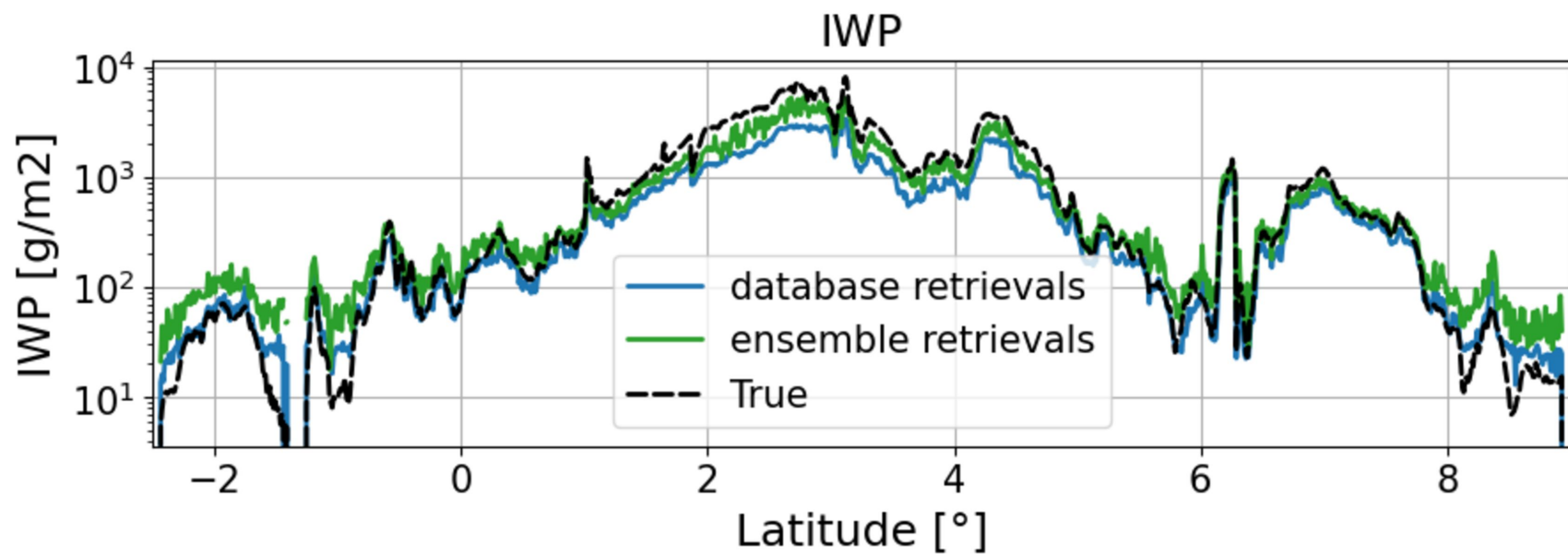
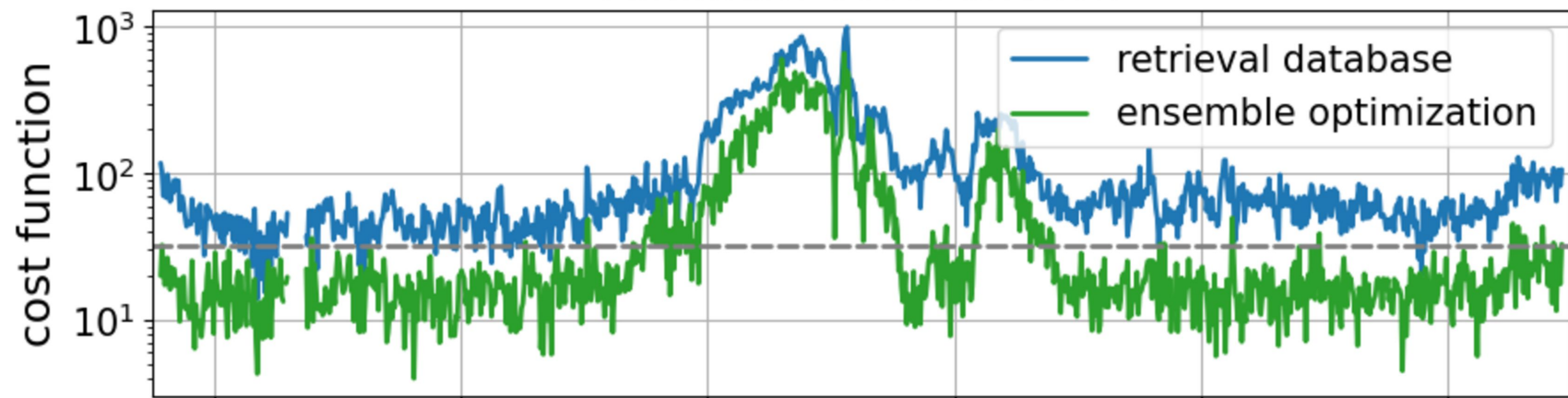
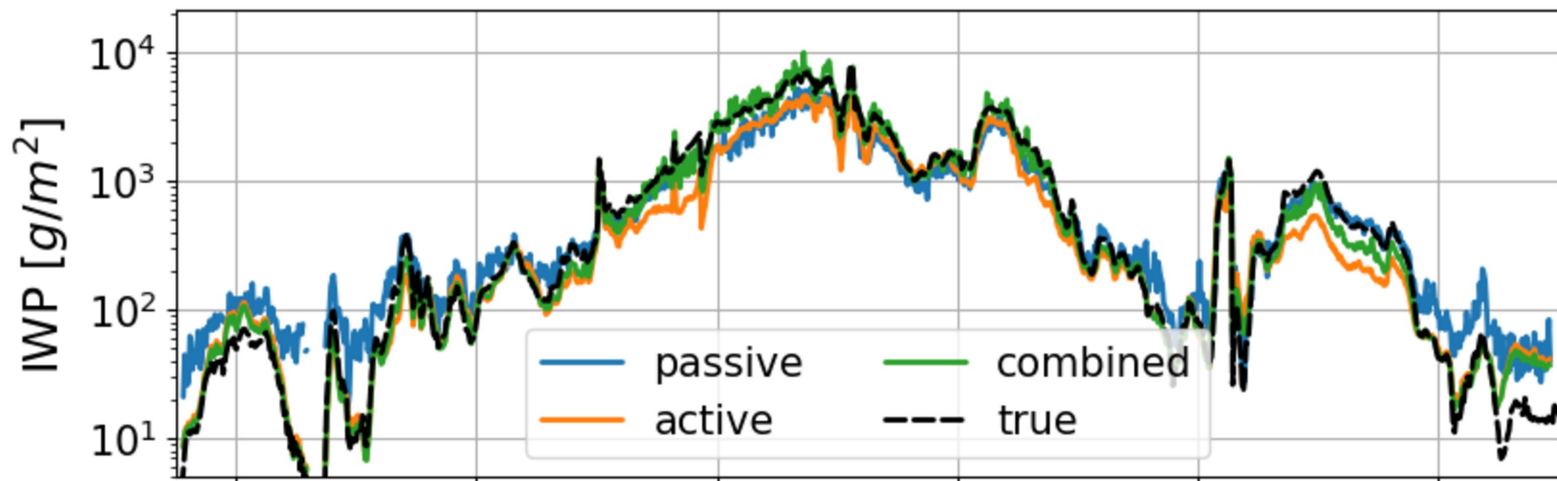


Figure11.

IWP



logarithmic IWP error

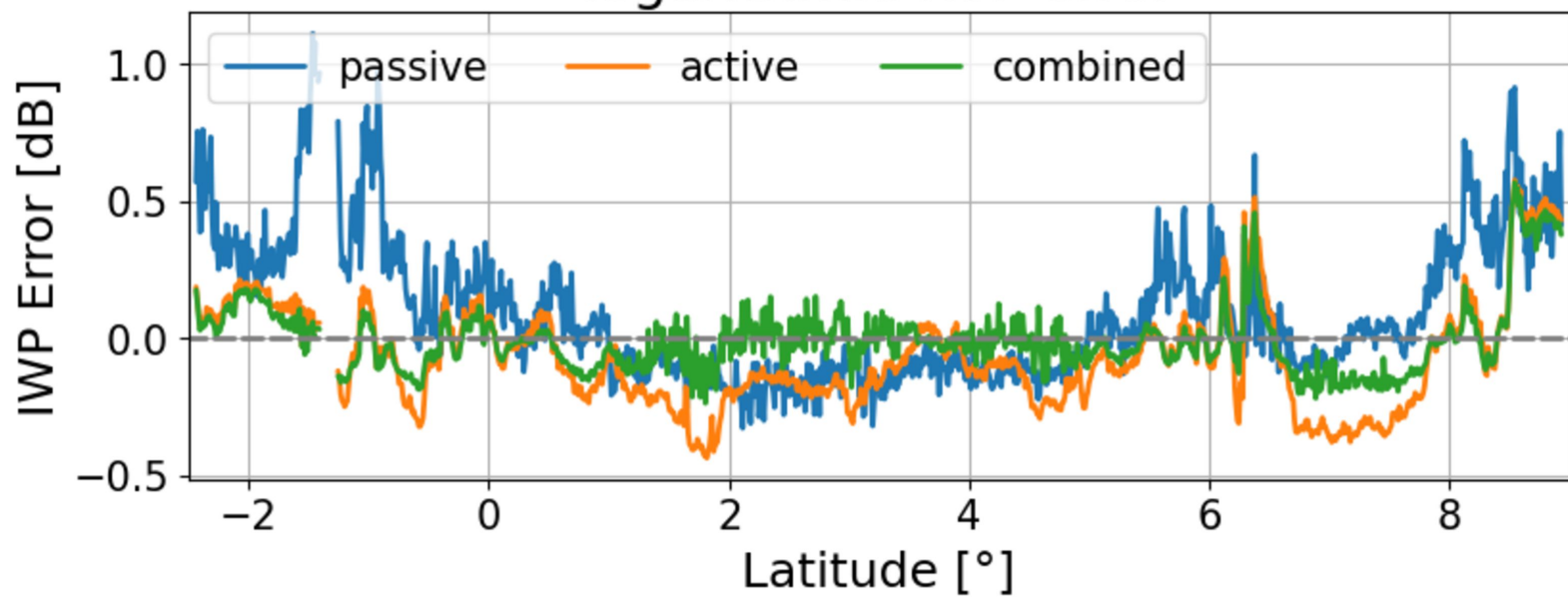


Figure12.

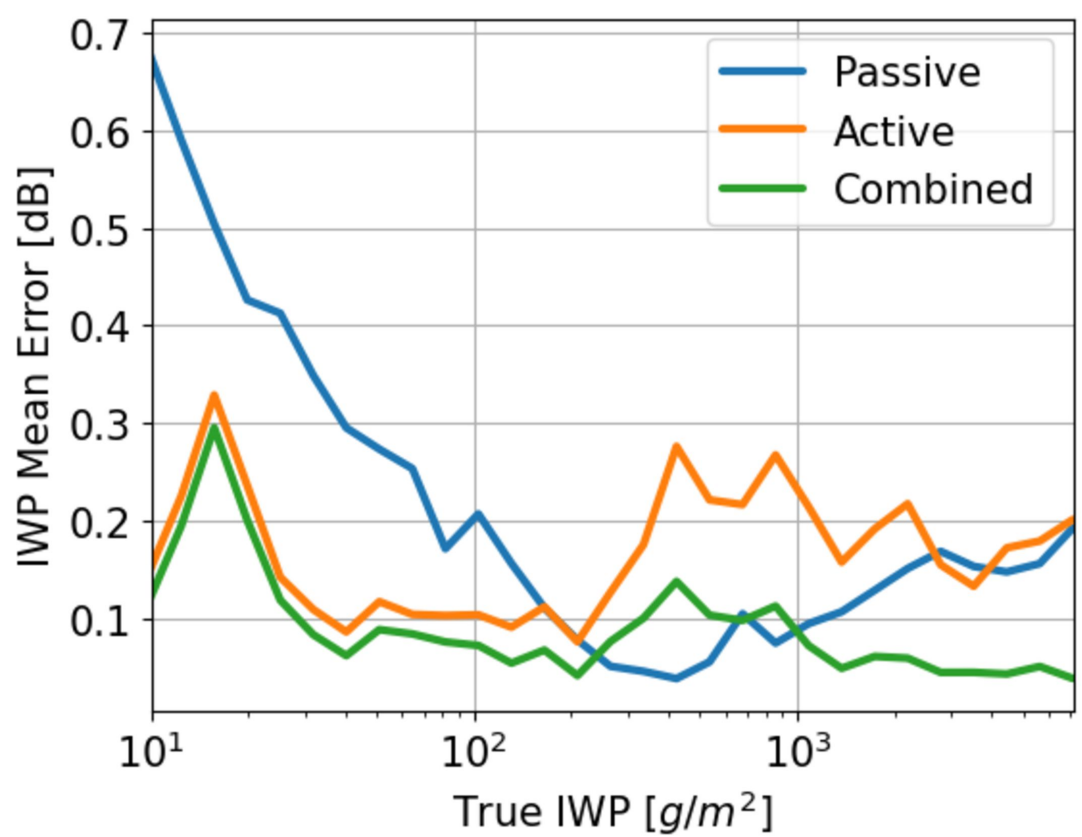


Figure13.

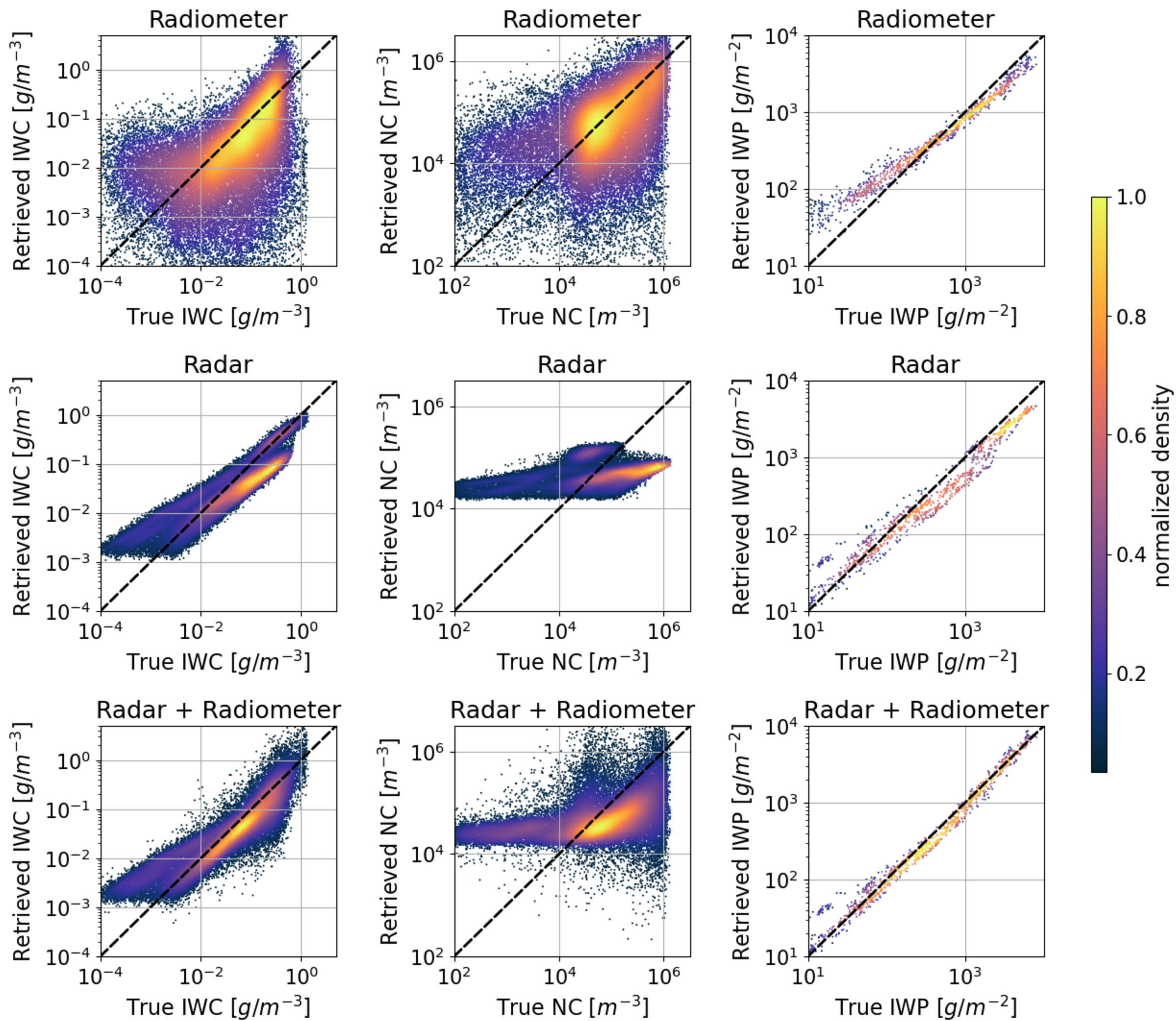
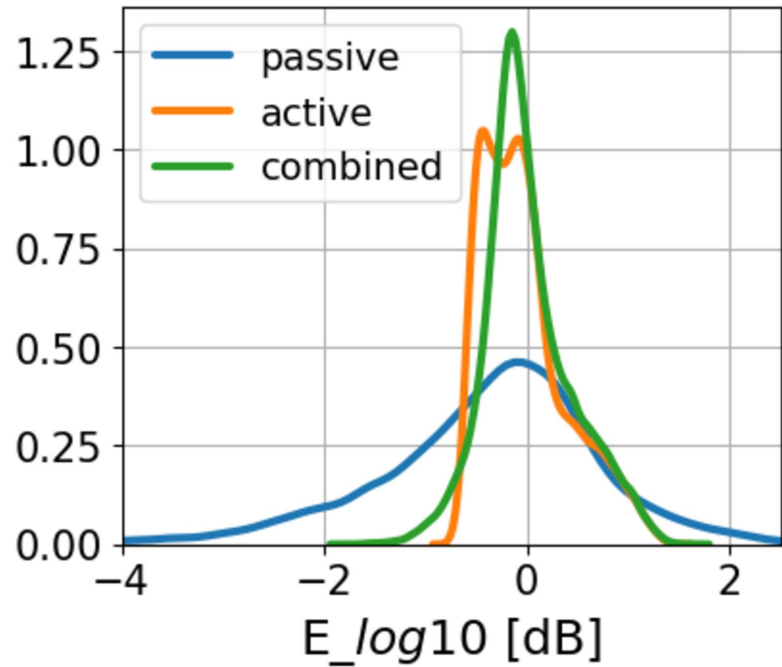
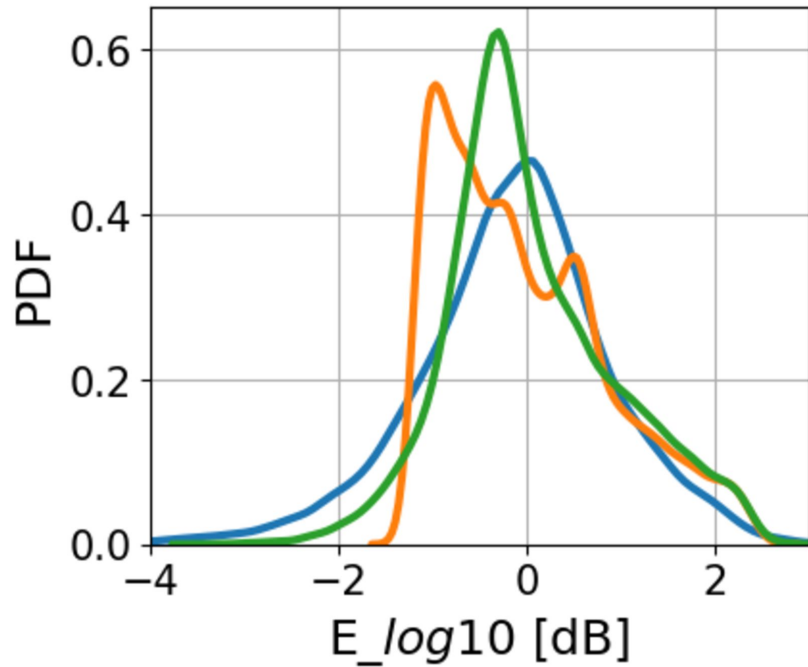


Figure14.

IWC



NC



IWP

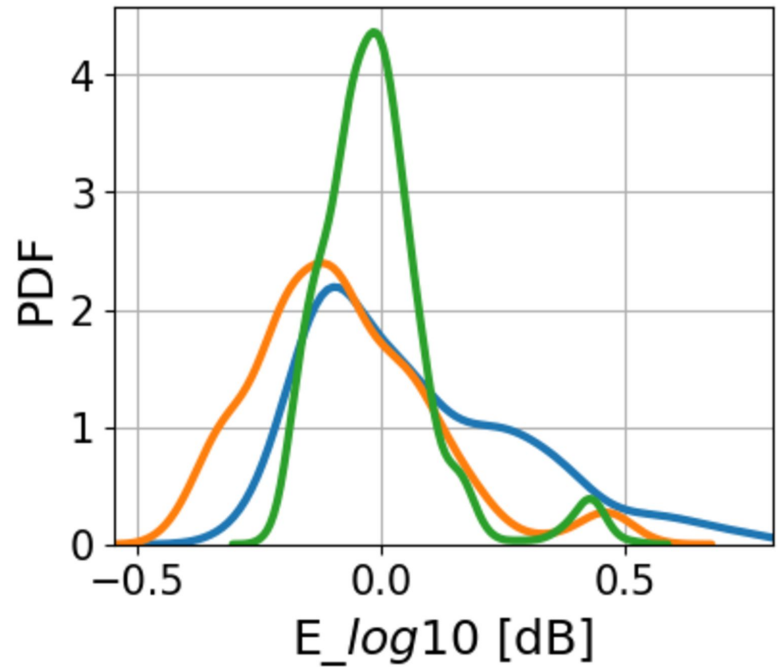


Figure15.

